

# **Test-Free Fracture Toughness**

Levon Minnetyan  
Clarkson University, Potsdam, New York 13699-5710

**Prepared under Grant NAG3-2394**

National Aeronautics and Space Administration  
Glenn Research Center

Final Report

January 2003

# TABLE OF CONTENTS

Acknowledgement.....	1
Abstract.....	2
Chapter I. Effects of Fiber Orientation on Fracture Toughness.....	3
1.1 Introduction.....	4
1.2 Methodology.....	5
1.3 Simulation of braided composite specimens.....	8
1.3.1 Fiber and Matrix Properties Calibration.....	9
1.4 Results and discussion.....	12
1.5 Conclusions.....	17
1.6 References for Chapter I.....	18
1.7 Figures for Chapter I.....	19
Chapter II. State-of-the-art of fiber-optic sensor systems	
in composite structures .....	29
2.1 Introduction.....	29
2.2 Fiber-optic sensors.....	30
2.2.1. Advantages over traditional NDI sensors.....	30
2.2.2. Categories of fiber-optic sensor system.....	31
2.2.3. General concerns on the fiber optic sensors.....	32
2.2.4. Installation of fiber-optic sensors.....	33
2.2.5. Survivability in curing process and fabricating process.....	34
2.2.6. Effects of embedded fiber optic sensor on material properties.....	35

2.2.6.1. <i>Coating types effects</i> .....	35
2.2.6.2. <i>Embedment location and direction</i> .....	36
2.2.6.3. <i>Strength loss by embedded fiber-optic sensors</i> .....	36
2.3 Applications of fiber-optic sensors.....	38
2.3.1. Strain measurement.....	38
2.3.2. Damage detection.....	42
2.3.3. Fatigue problems.....	42
2.3.4. Curing monitoring.....	44
2.3.5. Textile material test monitoring.....	45
2.4 Summary.....	46
2.5 Conclusion.....	49
2.6 References for Chapter II.....	49
Chapter III. Fiber optic sensor system in composite structures:	
computational simulation of damage propagation	
with embedded fiber-optic sensors.....	52
3.1 Introduction.....	52
3.2 Methodology.....	53
3.3 Simulation of coupons.....	56
3.3.1. Reference tensile specimen without embedded optical fiber.....	56
3.3.2. Specimen with parallel embedment of optical fiber.....	63
3.3.3. Specimen with perpendicular embedment of optical fiber.....	66

3.4 Discussion.....	68
3.5 Conclusions.....	72
3.6 References for Chapter III.....	73

## LIST OF TABLES

Table 1.1	Different specimen types and corresponding finite element mesh.....	8
Table 1.2	Specimen definition for fiber orientation.....	9
Table 1.3	ASZH Graphite Fiber Properties.....	11
Table 1.4	IMWM Epoxy Matrix Properties.....	12
Table 1.5	Computed W from simulation results of LB-A specimen.....	15
Table 1.6	Computational simulation results of short sharp notched specimens with different fiber orientation.....	17
Table 3.1	Kevlar 49® Fiber Properties.....	59
Table 3.2	Epoxy Matrix Properties.....	60
Table 3.3	Mechanical Properties of Unidirectional Kevlar 49®/Epoxy Laminate.....	61
Table 3.4	Glass Fiber Properties for Simulated Optical Fiber.....	62
Table 3.5	Comparison of Ultimate Strengths for Different Specimens between Simulations and Experiments (GPa).....	69
Table 3.6	Comparison of Composite Properties of Different Coupons.....	69
Table 3.7	Elastic Moduli Calculated from Structural Stress-Strain Relationship at different locations in Figure 3.11~3.14 (GPa).....	70

## LIST OF FIGURES

Figure 1.1	Specimen Geometry and Definition of parameters, $\phi$ is the notch-to-braid axis, $\beta$ is the braid angle.....	19
Figure 1.2.1	Finite element for Long specimen with blunt notch Total nodes 826, total elements 760.....	20
Figure 1.2.2	Finite element for Short specimen with blunt notch Total nodes 689, total elements 628.....	20
Figure 1.3	Refined finite element mesh at the notch tip for specimens with blunt notch.....	20
Figure 1.4.1	Finite element for Long specimen with sharp notch Total nodes 1012, total elements 936.....	21
Figure 1.4.2	Finite element for Short specimen with sharp notch Total nodes 715, total elements 650.....	21
Figure 1.5	Force vs. Displacement Curve.....	21
Figure 1.6	Percent Damage Volume with Loading.....	22
Figure 1.7	DERR vs Force.....	22
Figure 1.8	TDERR vs Force.....	22
Figure 1.9	Damage_Energy vs. Force.....	23
Figure 1.10	Damage_Energy vs. Damage .....	23
Figure 1.11	Updated finite element mesh after.....	24
Figure 1.12	Applied load in different stage vs. notch-to-braid axis angle For short sharp notched specimens.....	24
Figure 1.13.1	Final finite element mesh of SS-A specimen.....	25

Figure 1.13.2	Final finite element mesh of SS-B specimen.....	25
Figure 1.13.3	Final finite element mesh of SS-C specimen.....	26
Figure 1.13.4	Final finite element mesh of SS-D specimen.....	26
Figure 1.13.5	Final finite element mesh of SS-E specimen.....	27
Figure 1.14	Computed Damage_Energy vs. Notch angle for short sharp notched specimens.....	27
Figure 1.15	Applied load in different stages vs. notch angle for short blunt notched specimens.....	28
Figure 2.1(a)	Original optical fiber bonding.....	33
Figure 2.1(b)	Improved optical fiber bonding.....	33
Figure 2.2	Comparison of different methods of edge section displacement in the aluminum cantilever beam test.....	34
Figure 2.3	Comparison of tensile properties of pultruded CFRP and GFRP.....	37
Figure 2.4	Comparison of shear properties of pultruded CFRP and GFRP.....	37
Figure 2.5	Stress distributions in 0° and 45° ply of [02,-45,+45] <sub>s</sub> multiply laminate under tension tests.....	39
Figure 2.6a	Through- the-thickness strain distribution per unit loading in 8-ply laminate.....	40
Figure 2.6b	Through- the-thickness strain distribution per unit loading in 16-ply laminate.....	40
Figure 2.7	Compressive specimen with central embedded optic fiber.....	40
Figure 2.8(a)	1.0KN load, contour interval 0.1μm.....	41
Figure 2.8(b)	2.0KN load, contour interval 0.2μm.....	41

Figure 2.9	Global stress vs. average strain curve.....	41
Figure 2.10	Comparison of the fiber optic failure signal with PZT signal for a [904/04]s.....	43
Figure 2.11	Strain from extensometer and embedded Bragg Grating sensor in a FRP tendon subjected to a sinusoidal load.....	43
Figure 2.12	Strain vs. time plot from extensometer and Bragg Grating sensor in a glass tendon subjected to a sinusoidal load.....	44
Figure 2.13	Experimental results for strain measurement.....	45
Figure 3.1	Finite element mesh for the tension specimen.....	57
Figure 3.2	Boundary conditions and specimen dimensions.....	58
Figure 3.3	Final finite element mesh for the reference coupon.....	62
Figure 3.4	Damage progression for coupon with embedded optical fiber parallel to reinforcing fibers.....	64
Figure 3.5	Final finite element mesh for coupon with embedded optical fiber parallel to reinforcing fibers.....	64
Figure 3.6	Damage Percent vs. Load.....	65
Figure 3.7	Energy Release Rate vs. Load.....	66
Figure 3.8	Special elements for resin pocket in the specimen with embedded optical fiber perpendicular to the reinforcing fibers.....	66
Figure 3.9	Damage Percent vs. Total Load.....	67
Figure 3.10	Energy Release Rate vs. force.....	68
Figure 3.11	Over Structural Stress-Strain Relationship at Node 1.....	70
Figure 3.12	Over structural Stress-Strain Relationship at Node 2.....	71



Figure 3.13	Over Structural Stress-Strain Relationship at Node 3.....	71
Figure 3.14	Over Structural Stress-Strain Relationship at Node 4.....	72

## **Acknowledgements**

This report is the documentation of the work done at Clarkson University under NASA Grant No NAG3-2394 (Clarkson University Research Project No. 375-32634 with Old Number 375-563 prior to 7/1/2002). Project dates were July 1, 2000 to September 30, 2002 and total funding was \$70,554. The project monitor was Dr. Christos C. Chamis of Glenn Research Center. Many helpful discussions with Dr. Chamis on the implementation of this project are hereby acknowledged. The work reported herein is based on the thesis research of Mr. Wenming Zhao who is an MS student at Clarkson University and who also helped with the assembly of this report.

## **Abstract**

Computational simulation results can give the prediction of damage growth and progression and fracture toughness of composite structures. The experimental data from literature provide environmental effects on the fracture behavior of metallic or fiber composite structures. However, the traditional experimental methods to analyze the influence of the imposed conditions are expensive and time consuming. This research used the CODSTRAN code to model the temperature effects, scaling effects and the loading effects of fiber/braided composite specimens with and without fiber-optic sensors on the damage initiation and energy release rates. The load-displacement relationship and fracture toughness assessment approach is compared with the test results from literature and it is verified that the computational simulation, with the use of established material modeling and finite element modules, adequately tracks the changes of fracture toughness and subsequent fracture propagation for any fiber/braided composite structure due to the change of fiber orientations, presence of large diameter optical fibers, and any loading conditions.

## **Chapter I. Effects of Fiber Orientation on Fracture Toughness**

In this chapter biaxially braided compact tension C(T) specimens are evaluated by computational simulation via the Composite Durability STRuctural ANalysis (CODSTRAN) code. Damage progression characteristics as well as the ultimate structural fracture loads are computed and compared with test data. The effects of braid angle and the orientation of the braid axis with reference to the C(T) specimen notch direction are investigated with respect to their influences on damage and fracture progression characteristics. The braid angle is defined as internal angle between the two braid yarn orientations of a biaxial braid. The orientation of the braid axis is defined as the average of the orientations of the two braid tow directions. Several 4-step braided Graphite/Epoxy Mode I compact tension specimens are modeled and simulated. Both “long” and “short” versions of braided composite C(T) specimens are evaluated. Effects of sharp and blunt notches on damage initiation are also investigated. Results are depicted as force vs. displacement diagrams and the ultimate load vs. notch-to-tow angle diagrams. The simulated plots show good agreement with experimental data. Additionally, computational simulation is able to track the damage initiation, growth, and propagation processes at the microscopic level, enabling a more insightful interpretation of the test results. The final finite element models after the specimens are broken into two parts show the different fracture modes associated with the microscopic nodal and ply stresses due to the different fiber orientation and specimen dimensions. Results validate the computational simulation method and identify the damage initiation, growth, accumulation, and progressive fracture stages for braided composite C(T) specimens.

**Keywords:** textile composite materials, 3-D braided Graphite/Epoxy composite, C(T) specimen, notch angle, computational simulation, damage propagation

## 1.1 Introduction

Advanced textile-reinforced composites with braided or woven reinforced materials have anticipated and conjectured advantages over conventional composites such as two-dimensional and planar based conventional laminate- and fabric-reinforced composites in the properties of near net shape, high energy absorption, and the absence of delamination. Three-dimensional (3-D) composites are reinforced with three dimensional textile preforms, which are fully integrated continuous-fiber assemblies with multi-axial in-plane and out-of-plane fiber orientations.

These composites exhibit several distinct advantages that are not realized in traditional laminates. First, because of the out-of-plane orientation of some fibers, three-dimensional composites provide enhanced stiffness and strength in the thickness direction. Second, the fully integrated nature of fiber arrangement in three-dimensional preforms eliminates the inter-laminar surfaces characteristic of laminated composites. Third, the technology of textile preforming provides the unique opportunity of near-net-shape design and manufacturing of composite components and, hence, minimizes the need for cutting and joining the parts.

Previous research (Minnetyan, et al. 1997 and Huang, et al. 1998) has proven that computational simulations using the CODSTRAN code can be used to predict the influence of an existing notch, as well as loading on the safety and durability of fiber composite C(T) specimen and track the damage growth and propagation. Since the braid reinforced composite have many advantages over the conventional composite material and are used frequently in aerospace components and automobile components, it is essential to develop an effective computational capability to predict behavior of braided composite structures for any loading and geometry.

Present research models several 4-step braided Graphite/Epoxy C(T) specimens using CODSTRAN computational code. The basic unit of the 4-step structure used here can be viewed as tow sets of tow planes crossing one another and intersecting the braid axis at

equal angles (the braid angle  $\beta$ ). Both “long” and “short” versions of braided composite C(T) specimens are simulated. The effects of the orientation of the braid axis with reference to the C(T) specimen notch direction are investigated with respect to their influences on damage and fracture progression characteristics. Effects of sharp and blunt notches on damage initiation are also investigated. Results are depicted as force vs. displacement diagrams and the damage initiation load vs. notch-to-tow angle diagrams. A shell finite element model with refined mesh at the notch tip is used to track the process of such C(T) experiments. The final finite element model segments after the specimen breaks into two parts show different fracture modes that are affected by the microscopic nodal and ply stresses due to the different fiber orientations. Also, the results identify the damage initiation, growth, accumulation, and progressive fracture stages of such braided composite material C(T) specimens.

## **1.2 Methodology**

The CODSTRAN (COMposite Durability STRuctural Analysis) methodology, which was laid out by Chamis and Smith (1978) and developed by Minnetyan, Chamis, and Murthy (1997), is an open-ended, integrated and stand-alone computer code in Fortran. Its modular nature enables upgrading of nearly the entire code by replacing its modules. CODSTRAN has integrated the composite mechanics analysis (ICAN) and the finite element structural analysis (MHOST) codes as its computational modules. Computational simulation using CODSTRAN is comprised of three analysis modules: (1).micromechanics and macromechanics module (ICAN); (2).structural analysis module (MHOST); (3).damage progression tracking module.

Prior to each finite element analysis, the ICAN module utilizes a resident data bank that contains the typical fiber and matrix constituent properties, with provisions to add new constituents as they become available, and computes the composite properties and synthesizes the laminate generalized force-displacement relations according to the

composite lay-up. After each finite element analysis, ICAN helps determine whether or not the structure in its current state is in equilibrium under the applied loading and also helps evaluate the ability of composite structure to endure stresses and deformations due to additional loading increments.

The finite element analysis module uses the MHOST quadrilateral shell element load-displacement relations to accept the composite properties that are computed by the ICAN module and performs the structural analysis at each load increment with the equilibrium checks based on the allowable maximum number of damaged and fractured nodes during the application of a load increment. If too many nodes are damaged and fractured during a load increment, incremental loads are reduced and the analysis is repeated from the previous equilibrium stage. Otherwise, if there is an acceptable amount of incremental damage, the constitutive properties and the structural geometry are updated to account for the damage and deformations in the previous increment. Then, the load increment is kept constant and applied on the updated finite element mesh leading to possible damage and fracture. Analysis is stopped when global structural fracture is predicted or the specimen is broken into two pieces.

The overall evaluation of composite structural durability is carried out in the damage progression module that keeps track of composite degradation for the entire structure. After each finite element stress analysis, the following failure criteria are used to evaluate possible failure within each subvolume of each ply at each node of the composite structure:

$$S_{f11C} < \sigma_{f11} < S_{f11T}$$

$$S_{f22C} < \sigma_{f22} < S_{f22T}$$

$$S_{f33C} < \sigma_{f33} < S_{f33T}$$

$$S_{f12(-)} < \sigma_{f12} < S_{f12(+)}$$

$$S_{f23(-)} < \sigma_{f23} < S_{f23(+)}$$

$$S_{f13(-)} < \sigma_{f13} < S_{f13(+)}$$

The stress limits in above equations are computed by the ICAN module, based on constituent stiffness, strength, and fabrication process parameters. In addition to the first twelve failure modes, the thirteenth failure mode is a combined stress or modified distortion energy (MDE) failure criterion (Chamis 1969) that is obtained by modifying the usual distortion energy failure criterion expressed as

$$\left(\frac{\sigma_{\ell 11\alpha}}{S_{\ell 11\alpha}}\right)^2 + \left(\frac{\sigma_{\ell 22\beta}}{S_{\ell 22\beta}}\right)^2 - K_{\ell 12\alpha\beta} \frac{\alpha_{\ell 11\alpha}}{S_{\ell 11\alpha}} \frac{\sigma_{\ell 22\beta}}{S_{\ell 22\beta}} + \left(\frac{\sigma_{\ell 12S}}{S_{\ell 12S}}\right)^2 < 1$$

Where  $\alpha$  and  $\beta$  indicate tensile or compressive stresses,  $S_{\ell 11\alpha}$  is the local longitudinal strength in tension or compression,  $S_{\ell 22\alpha}$  is the transverse strength in tension or compression, and the directional interaction factor  $K_{\ell 12\alpha\beta}$  is defined as:

$$K_{\ell 12\alpha\beta} = \frac{(1 + 4\nu_{12} - \nu_{13})E_{22} + (1 - \nu_{23})E_{11}}{[E_{11}E_{22}(2 + \nu_{12} + \nu_{13})(2 + \nu_{21} + \nu_{23})]^{1/2}}$$

The directional interaction factor reduces to unity for homogeneous isotropic materials.

Once the damage modes at each node are assessed, a damage index is created to record the damage information for each damaged node. The damage index contains the node number, the ply number, and the list of damage criteria that have become activated. When a new failure occurs within a subvolume after a load increment, the damage index is updated correspondingly. The composite properties of each domain are degraded according to their damage index.

The damage progression module keeps a detailed account of composite degradation for the entire structure. It also acts as the master executive module that directs the composite mechanics module to perform micromechanics and macromechanics analysis/synthesis functions, and calls the finite element module with thick shell analysis capability to model composites for global structural response.



### 1.3 Simulation of braided composite specimens

The structural examples of this simulation, for which experimental results are available from the published literature by Filatovs et al. (1993), consist of several 3-D braid-reinforced Graphite/Epoxy C(T) specimens. The reported composite preforms are braided from tows containing 12 K (12000 individual fibers), 7  $\mu\text{m}$  diameter Ceylon G30-500 graphite fibers and braided by the 4-step process in  $3 \times 14$  patterns. The matrix is Epon828/T403 in a ratio of 100:42. Following mixing, the catalyzed resin is vacuum degassed. Through several steps of fabrication by vacuum compression, consolidation, and press cure in stainless steel mold, the resultant fiber volume fractions as determined by acid digestion per ASTM D-3171 were 48-50% with the void content  $<2\%$ .

The simulations contain different C(T) specimens with different dimensions of short version and long version. Different notch type of sharp by a razor blade and blunt notch with 0.25 mm radius semicircular (in **Table 1.1**) are evaluated. **Figure 1.1** shows the dimensions for these C(T) specimens.  $\beta$  is the braid angle defined as internal angle between two braid yarn orientations of biaxial braid, which is  $22^\circ$ .  $\phi$  is the notch angle between the notch-to-braid axis and Y coordinate. The orientation of the braid axis is defined as the average of the orientations of the two braid tow directions. To predict the influence on the damage initiation load and fracture toughness due to the different fiber orientations, several notch angles in **Table 1.2** are utilized for simulation of the short specimens with different notch types in this report.

**Table 1.1 Different specimen types and corresponding finite element mesh**

Type of specimen		SB	SS	LB	LS
Dimension type		Short	Short	Long	Long
Notch type		Blunt	Sharp	Blunt	Sharp
Finite element	Total nodes	689	715	826	1012
	Total elements	628	650	760	936

**Table 1.2 Specimen definition for fiber orientation**

<b>SPECIMEN LABEL</b>	<b>Notch angle <math>\phi</math></b>	<b>Grphite Fiber orientation</b>
-A	0	[68/-68/-68/68]
-B	22	[90/46/46/90]
-C	45	[23/67/67/23]
-D	68	[0/44/44/0]
-E	90	[22/-22/-22/22]

Quadrilateral shell finite elements are used to simulate the long and short specimens. **Figure 1.2.1** and **Figure 1.2.2** show the finite element meshes for specimens with blunt notch. A refined mesh (in **Figure 1.3**) is used to simulate the complicated stress and strain at the notch tip. Since the initiating crack extends beyond the notch tip, different finite element meshes are used to add the meshes around the initiating crack to model sharp notch specimens in **Figure 1.4.1** and **Figure 1.4.2**. Duplicate nodes with the same coordinates in the finite element model are used to represent the sharp initiating crack at the notch tip. They belong to separate elements and can deflect separately. The pin holes are not modeled in the finite element representation of the specimens to enable nodal support and loading. The finite element models are configured to have a node point at the center of each pin hole. One of the load points is restrained in all degrees of freedom except for  $\theta_z$ . The other load point is restrained only in  $D_y$ ,  $D_z$ ,  $\theta_x$ ,  $\theta_y$  directions, but allowed motion in X direction and rotation about the Z-axis. A concentrated tensile load in the X direction is applied at the node with freedom at X direction. The load is increased gradually.

### **1.3.1 Fiber and Matrix Properties Calibration**

To enable the programming simulation of such specimens using CODSTRAN code, it is necessary to identify the matrix and fiber properties and stress limits. Filatovs et al. (1993) only gave the experimental results of force vs. displacement relationships of LB-A

specimens and didn't provide the explicit matrix/fiber properties. The resident databank of the composite mechanics code provides properties of Graphite fiber and Epoxy matrix. Since only specified properties can match each of the specimens, the properties of fiber/matrix from the resident databank must be modified to match the experimental results via a least-squares error sum minimization method.

There are many properties of the fiber/matrix from the resident databank, which should be revised to match force versus displacement relation. Since Filatovs et al. reported the experimental results without consideration of hygrothermal behavior, we will keep the heat and moisture properties of the ASWV Graphite fiber and IMLS matrix as provided in the resident databank. The stiffness and strength properties of the fiber and matrix are obtained by calibrating the specific finite element model with the experimental data. Simulations of the LB-A specimen using finite element mesh in **Figure 1.2.1** can record any nodal displacement of each equilibrium stage during the damage and fracture propagation process. In the present study, only the displacement of the loaded node along the loading direction X is identified with respect to test data observed by Filatovs et al (1993). Computational simulation also records applied forces at each stage. The properties of fiber/matrix are revised and the specimens are simulated again if the errors of computed forces and the observed forces regarding with the recorded displacements between simulated results and experimental data are greater than acceptable. However, because of the natural complexity of the composite material, as well as the uncertainty and variability of experimental observations, it is not possible to obtain exactly the same computed values as the experimental results.

The difference between the observed and computed force is compared using the root-mean-square relative error sense for the recorded displacement points. The root-mean-square relative error  $\Omega$  was defined as:

$$\Omega = \sqrt{\frac{1}{n} \sum_{i=1}^n \left( \frac{F_i^{observed} - F_i^{computed}}{F_i^{observed}} \right)^2}$$

Where  $F_i^{observed}$  is value of observed force from the experiment which is compared with each recorded displacement in simulation,  $F_i^{computed}$  is the value of the same force computed from each equilibrium stage in simulation,  $n$  is the number of equilibrium stages in simulation. The smaller the value of  $\Omega$ , the better the agreement of force vs. displacement relations between simulation and experiment, and therefore more accurately identified are the fiber and matrix properties. The fiber and matrix properties identified by minimizing  $\Omega$  are given in **Table 1.3** and **Table 1.4**. Simulation results of LB-A specimens based on the properties in **Table 1.3** and **Table 1.4** gave a good agreement of the force vs. displacement relations as shown in **Figure 1.5**. The root-mean-square relative error  $\Omega$  of the forces was 2.66%.

**Table 1.3. ASZH Graphite Fiber Properties**

Number of fibers per end = 12000
Fiber diameter = 0.00699 mm (0.275E-3 in)
Fiber Density = 4.04E-7 Kg/m <sup>3</sup> (0.063 lb/in <sup>3</sup> )
Longitudinal normal modulus = 36.17 GPa (5.25E+6 psi)
Transverse normal modulus = 2.96 GPa (4.295E+5 psi)
Poisson's ratio ( $\mu_{12}$ ) = 0.10
Poisson's ratio ( $\mu_{23}$ ) = 0.10
Shear modulus ( $G_{12}$ ) = 21.37 GPa (3.10E+6 psi)
Shear modulus ( $G_{23}$ ) = 4.00 GPa (0.58E+6 psi)
Longitudinal thermal expansion coefficient = -1.0E-6/°C (-0.55E-6/°F)
Transverse thermal expansion coefficient = 1.0E-5/°C (0.56E-5/°F)
Longitudinal heat conductivity = 0.302 J-m/hr/m <sup>2</sup> /°C (4.03 BTU-in/hr/in <sup>2</sup> /°F)
Transverse heat conductivity = 0.0302 J-m/hr/m <sup>2</sup> /°C (0.403 BTU-in/hr/in <sup>2</sup> /°F)
Heat capacity = 712 J/Kg/°C (0.17 BTU/lb/°F)
Tensile strength = 3,454 MPa (501 ksi)
Compressive strength = 2,703 MPa (392 ksi)

**Table 1.4. IMWM Epoxy Matrix Properties:**

Matrix density = 0.0460 lb/in <sup>3</sup>
Normal modulus = 685 MPa (99.5 ksi)
Poisson's ratio = 0.410
Coefficient of thermal expansion = 0.57E-4/°F
Heat conductivity = 8.681E-3 BTU-in/hr/in <sup>2</sup> /°F
Heat capacity = 0.25 BTU/lb/°F
Tensile strength = 66.53 MPa (9.65 ksi)
Compressive strength = 68.94 MPa (10.0 ksi)
Shear strength = 67.57 MPa (9.80 ksi)
Allowable tensile strain = 0.042
Allowable compressive strain = 0.042
Allowable shear strain = 0.032
Allowable torsional strain = 0.032
Void conductivity = 16.8 J-m/hr/m <sup>2</sup> /°C (0.225 BTU-in/hr/in <sup>2</sup> /°F)
Glass transition temperature = 216°C (420°F)

## **1.4 Results and discussion**

Since all the specimens using the specified material properties have similar simulation procedure, only the LB-A [68/-68] s specimen is discussed in detail here. The load starts from 4.448N (1.0 lb.) at the movable node 666 and increases gradually. **Figure 1.6** shows the simulated relationship between structural percent damage and the applied loading. Damage initiation stage corresponds to the development of a damage zone around the notch tip by transverse tensile damage due to matrix failure. When the load reaches 215.7N (48.5 lb.), damage is detected at the node 387 of the matrix tensile failure in the outer ply. With the additional increase of the loading, matrix fractures expand from one ply to other plies. At the 618.3N (139 lb.) loading, fiber fracture occurs due to the longitudinal compression failure, indicating conclusion of the damage initiation stage. After that, ply transverse tensile fracture grows into through-the-thickness cracks at the notch tip. A prominent structural damage growth occurs though only a very small load increment is applied. Then, critical damage stage occurs before the load reaches 653.9N

(147 lb.). As the load is further increased gradually, the damage volume rises rapidly and indicates damage propagation stage, in which a small load increment causes more deflection of the specimen than in damage initiation stage. Consequently, as a lower slope occurs in the force and displacement relationship shown in **Figure 1.5**. The 824.67N (185 lb.) load is the maximum equilibrium load. After this load, the specimen enters an unstable fracture propagation stage. The load cannot be increased above 185 lb. without fracturing the specimen. When the load is increased to 831.8 N (187 lb.), the specimen is broken into two pieces.

**Figure 1.7** shows the relationship between load and the damage energy release rate (DERR) from simulation results of LB-A specimen. **Figure 1.8** shows the total damage energy release rate (TDERR) as a function of the applied forces. The DERR is defined globally as the increased work done by applied forces in each stage, per unit damage volume produced during structural degradation. TDERR is computed as the ratio of total damage energy to the corresponding total damage volume. Both TDERR and DERR can be used to evaluate structural resistance against damage propagation at different stages of loading and evaluate the composite fracture toughness. Typically, at the stage of damage initiation, there is a high rate of energy release that dissipates a significant portion of the strain energy stored in the composite structure. For LB-A specimen, the TDERR and DEER reach the highest value in **Figure 1.7** at 215.7N (48.5 lb.) load that corresponds to damage initiation. After that, the lower values of the DERR and TDERR means the ability of the structure to resist damage is decreased. The minimum value in both diagrams indicates that the maximum load for damage tolerance is 631.6N (142 lb.). After this, damage propagated more rapidly as the ultimate load was reached.

**Figure 1.9** shows the relationship of damage-energy and applied forces. Damage energy is also plotted as function of the produced structural percent damage in **Figure 1.10**. Damage energy increased greatly after the load level of 618.3N (139 lb.) as well as the damage volume increased sharply as shown in **Figure 1.6**. This rapid damage increase corresponds to the creation of through-the-thickness cracks at the notch tip. After

reaching the peak value at 689.0N (155lb.) loading, the damage energy cannot increase anymore until the simulated specimen is broken into two parts.

Fracture toughness can be evaluated by many methods such as average fracture energy and strain energy release rate. Filatovs et al. (1993) used the quantity designated as  $W$  to define the work of fracture as the fracture characterizing parameter.  $W$  was defined as the energy per unit area of fracture surface consumed in fracture progression:

$$W = \int P du / A \quad (1)$$

Where  $P$  is the load,  $u$  the displacement of the load, and  $A$  the corresponding crack area. The numerator is the energy absorbed by the specimen and is the envelope of the force vs. displacement curve in **Figure 1.5**. The simulation results of LB-A specimen provide the fundamental data to analyze the fracture behavior such as damage volume, energy release rate, and instantaneous/incremental values. Therefore,  $W$  can also be obtained from damage energy, TDERR, and DERR in **Figure 1.6~1.8**, respectively, using the following expressions:

$$W = \frac{\text{Damage\_energy}}{\text{CrackArea}} \quad (2)$$

$$W = \frac{\text{TDERR} \times \text{Damage\_Volume}}{\text{CrackArea}} \quad (3)$$

or

$$W = \frac{\sum \text{DERR} \times \text{Damage\_increment}}{\text{CrackArea}} \quad (4)$$

Where Damage\_Volume can be calculated from the percent damage in each stage multiplied by structural volume. Crack area is expressed as  $A = n \times l \times t$ , where  $l$  is the crack extension from the notch tip,  $t$  is the thickness, and  $n$  is a correction factor to account for the area increase due to path tortuosity by experiment. In the fracture propagation stage, the value of  $n$  is identified as 6 by Filatovs et al (1993). **Figure 1.11** shows the updated finite element mesh at the critical state of structural damage occurring after the 631.6N (142lb.) loading. Computed crack area is  $198 \text{ mm}^2$ , which is between  $100 \text{ mm}^2$  and  $200 \text{ mm}^2$  reported by the literature for different specimens. **Table 1.5**

shows computed  $W$  from simulation results using different methods, which are higher than the test result specified as 550~600 J/m<sup>2</sup>.

**Table 1.5. Computed  $W$  from simulation results of LB-A specimen**

Methods	(1)	(2)	(3)	(4)
Simulation $W$ (J/m <sup>2</sup> )	1263	3075	924	924

Simulations of short specimens with sharp notches using the finite element mesh shown in **Figure 1.3.2** show strong fiber orientation effects on the structural behavior during fracture processes. **Table 1.6** compares the simulation results with different fiber orientation in each damage stage of damage initiation, damage growth and damage propagation. Computational results record each equilibrium load during simulation. The quantity of damage initiation load in simulation is identified between the load before damage and load at the damage initiation. Ultimate load refers to the maximum equilibrium load since the specimen will be broken into two parts after this loading level. SS-A specimen ( $\phi=0^\circ$ ) has the lowest damage initiation load, which is nearly half of the highest one of SS-E specimen though they have close values of their ultimate load. **Figure 1.12** shows the variation of the damage initiation load and of the ultimate load as functions of the notch-to-braid axis angle. The damage initiation load ranges from experimental results are also depicted in **Figure 1.12**. All simulated damage initiation loads fall in the ranges except for the applied load for SS-E specimen, which is somewhat lower than the observed results. However, the damage initiation load increase as the notch angle  $\phi$  increases, which is consistent with the test observations.

**Figure 1.13.1~1.13.5** display the final finite element meshes after the short specimens with sharp notches have been broken into two parts. Structural fracture tendency shows a strong sensitivity to fiber orientation even though there is the same mechanism of transverse tension failure in matrix ( $\sigma_{t22, T}$  in **Table 1.6**) before the evolution of through-the-thickness cracks. For SS-A specimen in **Figure 1.13.1**, the progressive fracture



propagated along the 68° and –68° fiber orientation, and the structural fracture occurred at 90° to the notch-to-braid axis angle. For SS-B specimen in **Figure 1.13.2**, notch direction was parallel to the 90° tow planes and the 46° cross planes caused the severe damage. Other specimens also had the similar fracture progression characteristics. Such functional dependency shown by **Figure 1.12** and **Figure 1.13** supports the observation that tow planes are the most frequent planes of failure in compact tension testing. That is, after the initial crack at the sharp notch tip, progressive fracture extends mainly along the tow plane orientation, which finally results in the abrupt structural fracture.

Damage energy as a parameter of fracture toughness is also calculated for short sharp-notched specimens with different fiber orientations. We can get damage energy directly from the output file or calculate it by following equations:

$$Damage\_Energy = TDERR \times Damage\_volume$$

$$Damage\_Energy = \sum DERR \times Damage\_increment$$

or

$$Damage\_energy = \int P \times du$$

**Figure 1.14** shows the computed damage energy using different methods as function of the notch angles. Three methods have the same variation tendency with regard to the effect of the notch angle except for the damage energy obtained directly from the output files.

Short specimens with blunt notch are also simulated using finite element model shown in **Figure 1.2.2**. **Figure 1.15** exhibits variation of the applied load with respect to notch-to-braid axis angles. Damage initiation loads and ultimate loads of such short blunt notch specimens show less sensitivity on the different fiber orientation except for SB-E specimen with notch angle  $\phi=90^\circ$  has highest ultimate load nearly double of the minimum one.

**Table 1.6 Computational simulation results  
of short sharp notched specimens with different fiber orientation**

Specimen type		SS-A	SS-B	SS-C	SS-D	SS-E
Notch angle $\phi$ (degree)		0	22	45	68	90
Fiber Orientation (degree)		68/-68	90/46	23/67	0/44	22/-22
Damage initiation	Failure mode Mechanism	$\sigma_{f22, T}$	$\sigma_{f22, T}$	$\sigma_{f22, T}$	$\sigma_{f22, T}$	$\sigma_{f22, T}$
	Load before damage (N)	73.4	144.6	168.1	231.7	144.6
	Load at damage (N)	144.6	168.1	215.7	263.3	286.9
Damage Growth	Failure mode Mechanism	$\sigma_{f22, T}$	$\sigma_{f22, T}$	$\sigma_{f11, C}$ $\sigma_{f22, T}$	$(\sigma_{f11, T})$ $\sigma_{f22, T}$ $\sigma_{f12, (-)}$	$\sigma_{f22, T}$
	Load (N)	168.1	215.7	231.6	273.6	334.5
Damage propagation	Failure mode Mechanism	$\sigma_{f22, T}$	$\sigma_{f22, T}$	$\sigma_{f11, C}$ $\sigma_{f22, T}$	$(\sigma_{f11, T})$ $\sigma_{f22, T}$ $(\sigma_{f12, (-)})$	$\sigma_{f22, T}$
	Ultimate load (N)	334.0	379.0	300.9	282.9	381.6
Unstable damage propagation	Mechanism	$\sigma_{f11, T}, \sigma_{f11, C}$ $\sigma_{f22, T}, \sigma_{f22, C}$ $\sigma_{f12, (+)}, \sigma_{f12, (-)}$	$\sigma_{f11, T}, \sigma_{f11, C}$ $\sigma_{f22, T}, \sigma_{f22, C}$ $\sigma_{f12, (+)}, \sigma_{f12, (-)}$	$\sigma_{f11, T}, \sigma_{f11, C}$ $\sigma_{f22, T}, \sigma_{f22, C}$ $\sigma_{f12, (+)}, \sigma_{f12, (-)}$	$\sigma_{f11, T}, \sigma_{f11, C}$ $\sigma_{f22, T}, \sigma_{f22, C}$ $\sigma_{f12, (+)}, \sigma_{f12, (-)}$	$\sigma_{f11, T}, \sigma_{f11, C}$ $\sigma_{f22, T}, \sigma_{f22, C}$ $\sigma_{f12, (+)}, \sigma_{f12, (-)}$
Variation range of experimental damage initiation load (N)		100~175	80~150	85~195	185~275	370~415

## 1.5 Conclusions

Several 3-D Graphite/Epoxy composite Mode 1 compact tension specimens are simulated using the CODSTRAN computational simulation results. A quantitative estimate of the initiation load and work of fracture have been evaluated. The significant results from these investigations in which computational simulation was used to evaluate damage growth and propagation to fracture for such specimens are as follows:

1. Computational simulation, with the use of established composite mechanics and finite element modules, can be used to predict the influence of an existing notch, as well as loading on the progressive fracture of the composite specimens.
2. Computational simulation adequately tracks the damage growth and subsequent propagation to fracture for composite compact tension specimens.
3. Computational simulation provides detailed information on damage initiation and progression mechanisms, as well as identifying sensitive material parameters affecting structural fracture and fracture toughness.
4. Simulation results of LB-A specimen using the CODSTRAN code with the established finite element model show a good agreement with the experimental data on the force and displacement relationship.
5. Simulation results of short sharp-notched specimens can evaluate the sensitivity of damage initiation load and fracture toughness on fiber orientation. Specimens with lower notch angle  $\phi$  always correspond to lower damage initiation load.
6. The damage initiation is more sensitive to the variation of fiber orientation for the specimens with initial crack at the notch tip than the blunt notched specimens.
7. Ultimate load is less sensitive on fiber orientation since the same fiber tension or compression failure mode causes the finally structural fracture along the frequent failure plane, the tow plane direction.

## 1.6 References for Chapter I

Filatoves, G.J. and Sadler, R.L. and EL-Shiekh, H.M. 1993, "Fracture Behavior of a 3-D Braid Graphite/Epoxy Composite", J. of Composite material, Vol. 28, No.6/1994, pp. 527-543

Huang, D., and Minnetyan, L., and P.E. Member, ASCE, 1998, "Damage Progression in Carbon-Fiber Reinforced Plastic I-Beams", J. of Composite for Construction, February, 1998, pp.38-45

Minnetyan, L., and Chanis, C.C. 1997, "The Compact Tension, C(T), Specimen in Laminate Composite Testing", Composite Material: Fatigue and Fracture, Sixth Volume ,

ASTM STP 1285, E.A. Armanios, Ed., American Society for Testing and Materials, 1997, pp. 531-550

Minnetyan, L. 1997, "Composite Durability STRuctural ANalysis (CODSTRAN) USER'S MANUAL"

Minnetyan, L. "Test-Free Fracture Toughness", Submitted to NASA Glenn Research Center, Cleveland, Ohio

Murthy, P.L.N. and Chamis, C.C. 1986 "Integrated Composite Analyzer (ICAN): Users' and Programmers Manual", NASA Technical Paper 2515

Nakazawa, S. and Spiegel, M.S. 1987, "MHOST Users' Manual", Prepared for NASA Lewis Research Center by MARC Analysis Research Corp., April

Zhang, H. and Minnetyan, L. and Chamis, C.C. and Abdi, F. 2001, "Microstress Level Damage Evaluation in Composite Structures", Published by Society for the Advanced of Material and Process Engineering with Permission.

## 1.7 Figures for Chapter I

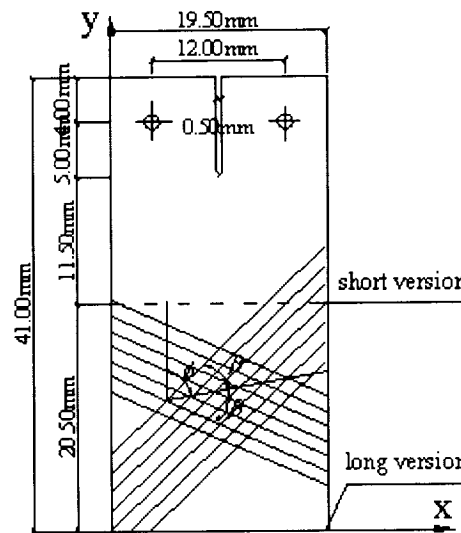


**Figure 1.1 Specimen Geometry and Definition of parameters,  $\phi$  is the notch-to-braid axis,  $\beta$  is the braid angle**

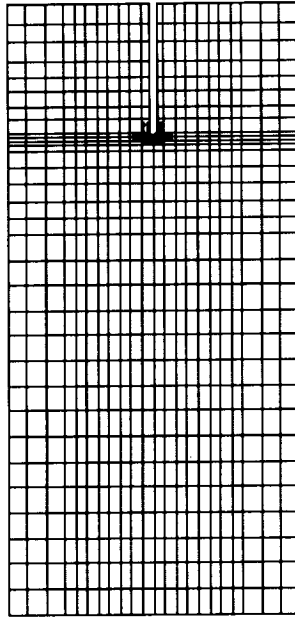


**Figure 1.2.1 Finite element for Long specimen with blunt notch**  
Total nodes 826, total elements 760

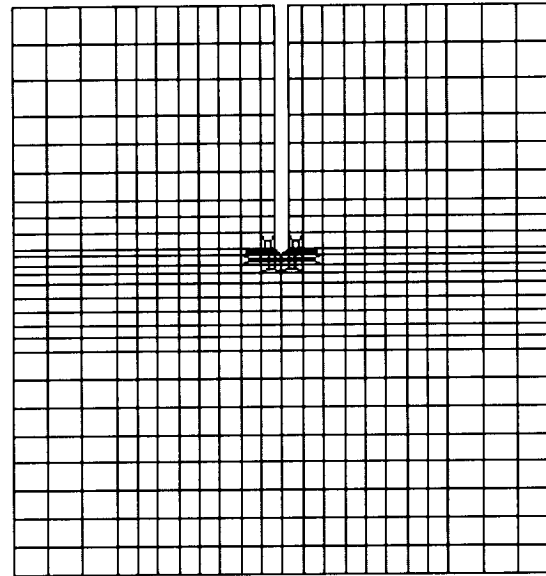


**Figure 1.2.2 Finite element for Short specimen with blunt notch**  
Total nodes 689, total elements 628

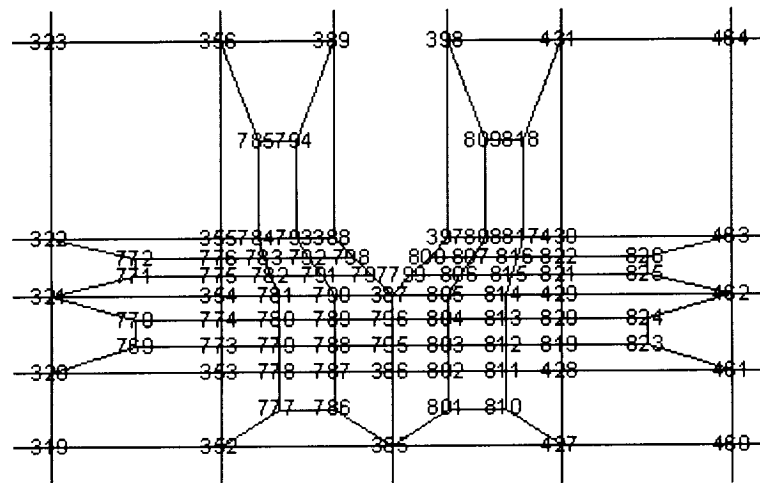


**Figure 1.3 Refined finite element mesh at the notch tip for specimens with blunt notch**

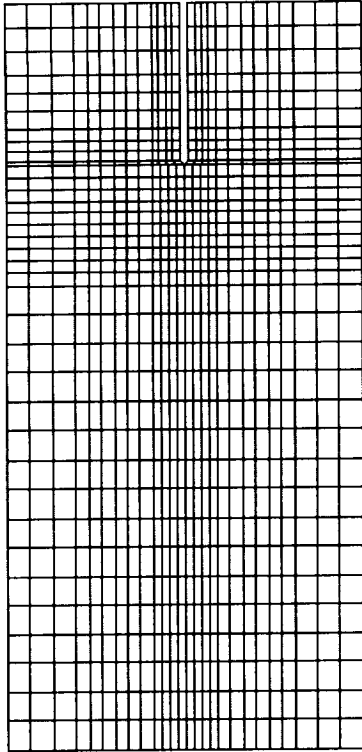


**Figure 1.4.1** Finite element for Long specimen with sharp notch  
Total nodes 1012, total elements 936

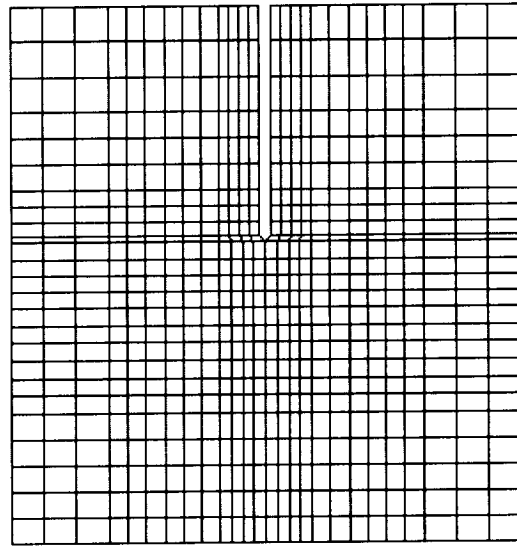


**Figure 1.4.2** Finite element for Short specimen with sharp notch  
Total nodes 715, total elements 650

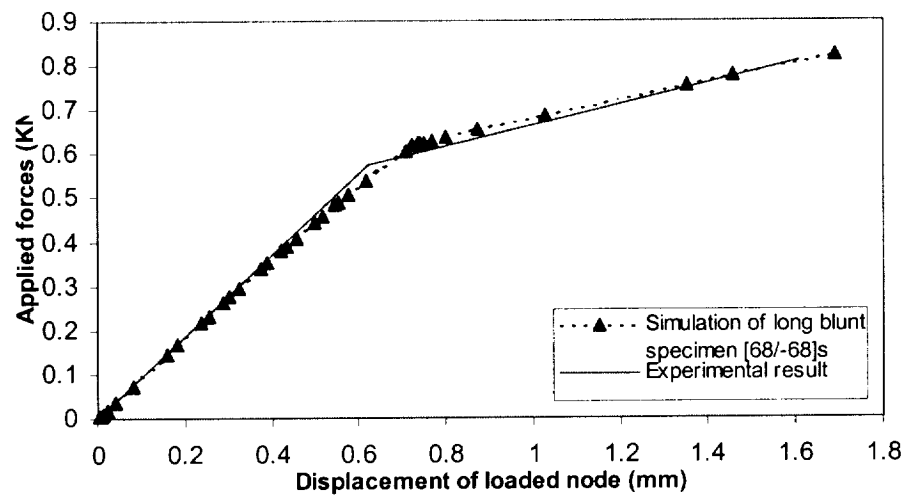


**Figure 1.5** Force vs. Displacement Curve

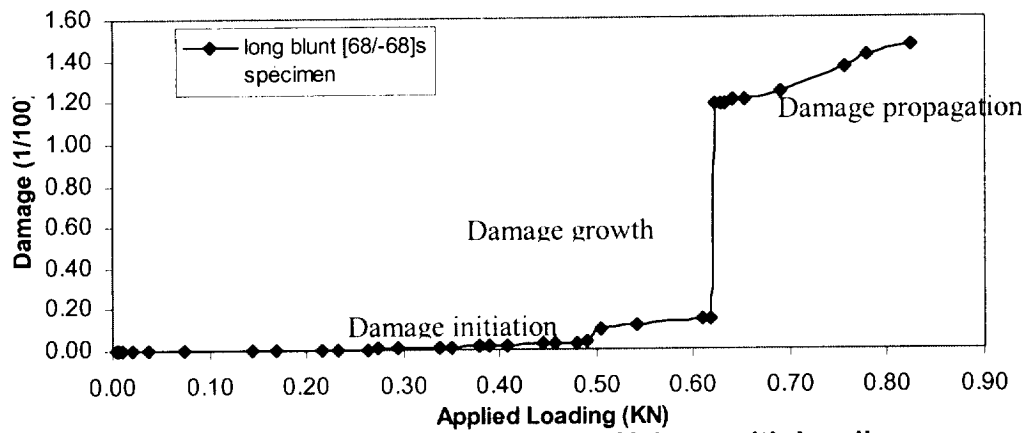


Figure 1.6 Percent Damage Volume with Loading

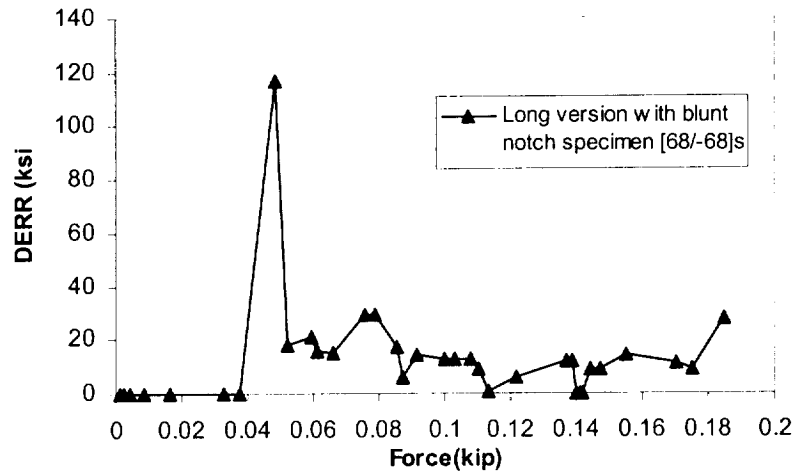


Figure 1.7 DERR vs Force

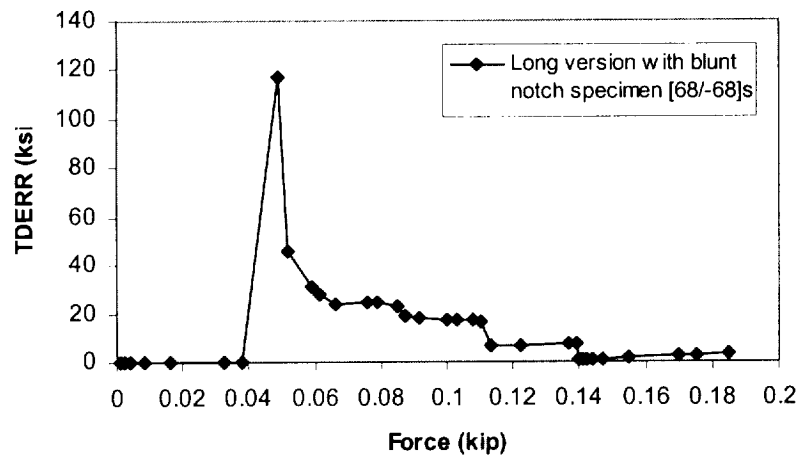


Figure 1.8 TDERR vs. Force

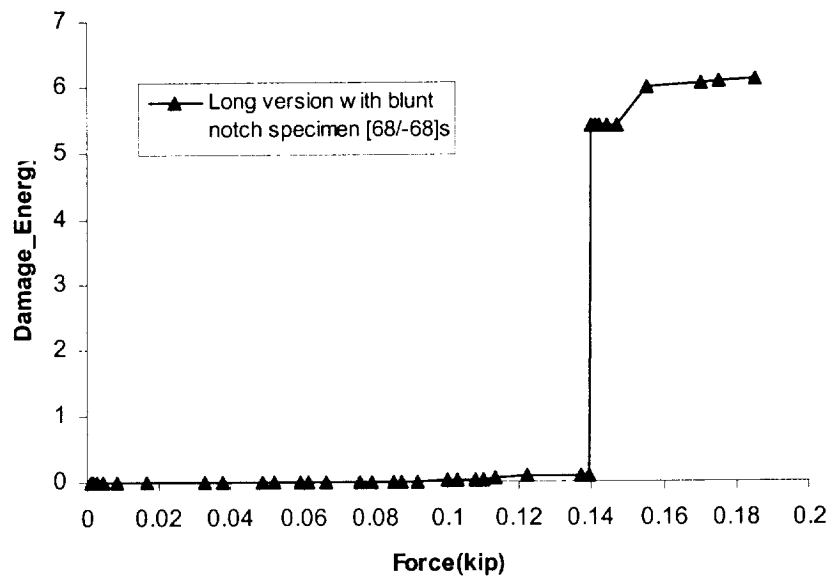


Figure 1.9 Damage\_Energy vs. Force

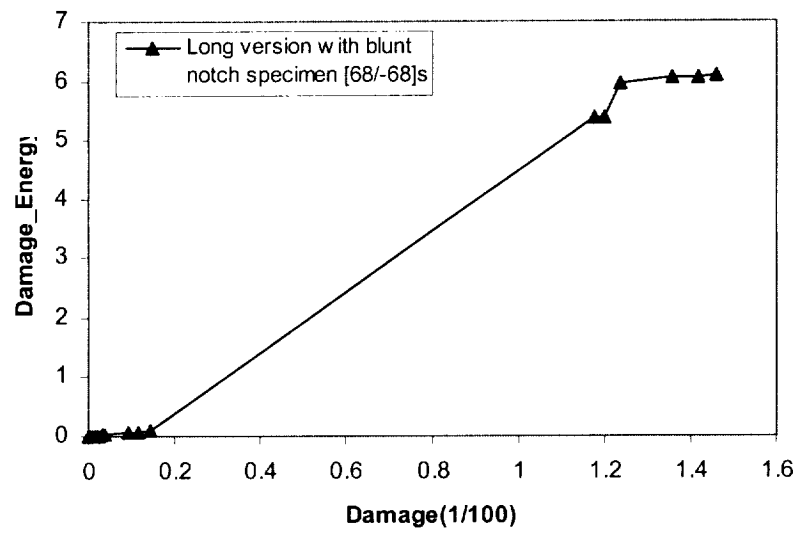
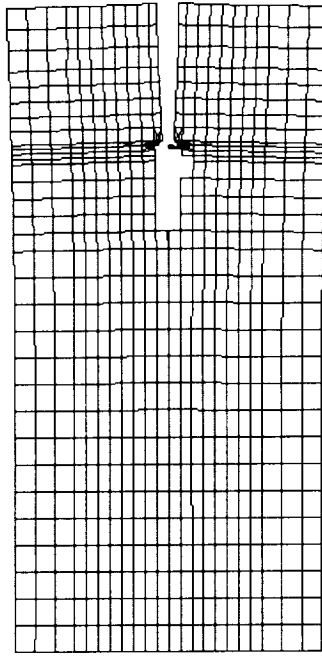
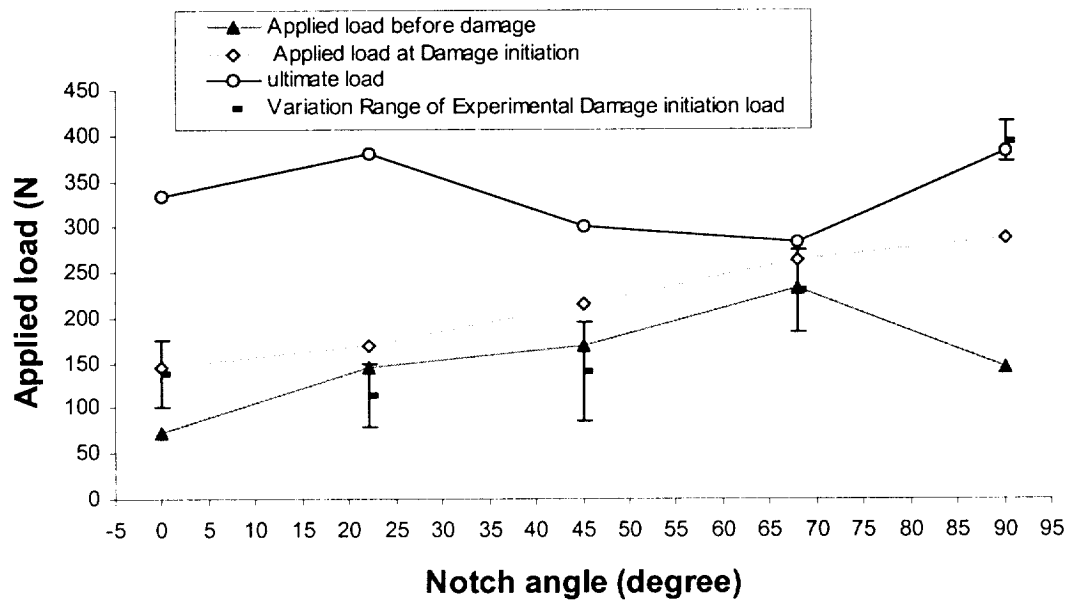


Figure 1.10 Damage\_Energy vs. Damage





**Figure 1.11 Updated finite element mesh after the critical damage stage for LB-A specimen**



**Figure 1.12 Applied load in different stage vs. notch-to-braid axis angle For short sharp notched specimens**

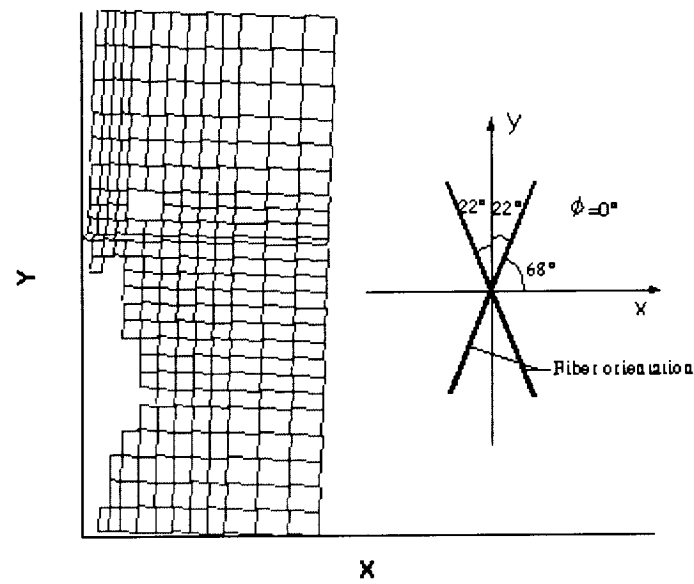


**Figure 1.13.1 Final finite element mesh of SS-A specimen**

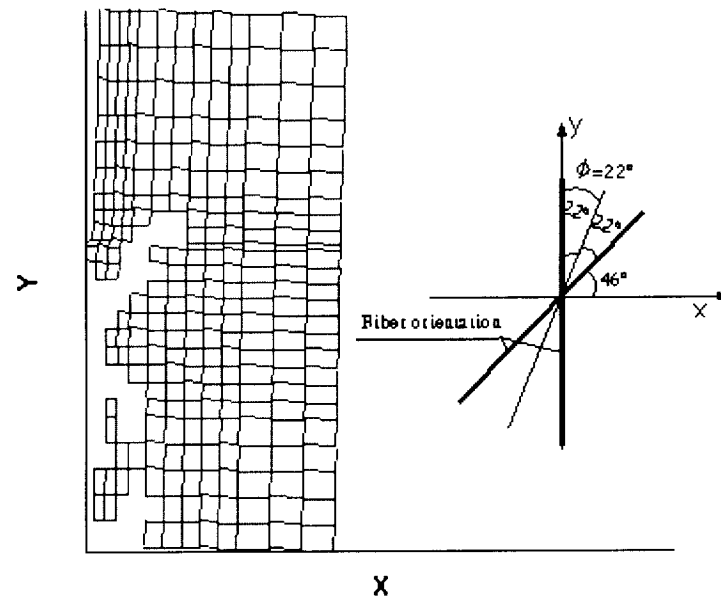


**Figure 1.13.2 Final finite element mesh of SS-B specimen**

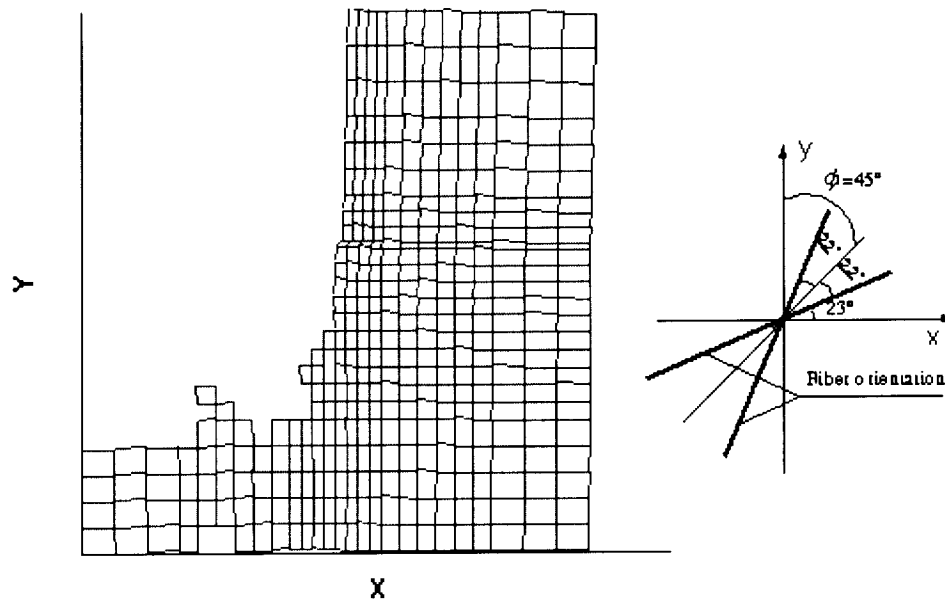


**Figure 1.13.3 Final finite element mesh of SS-C specimen**

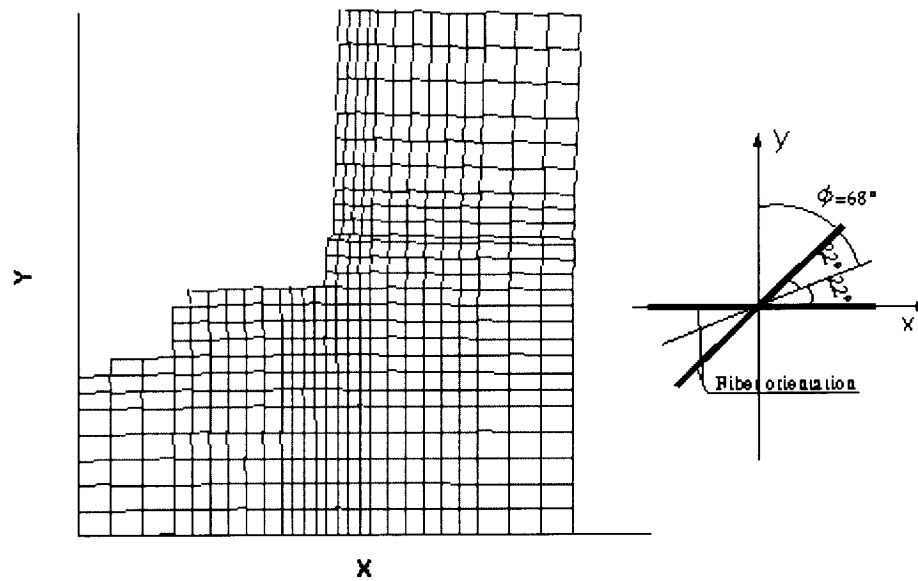


**Figure 1.13.4 Final finite element mesh of SS-D specimen**

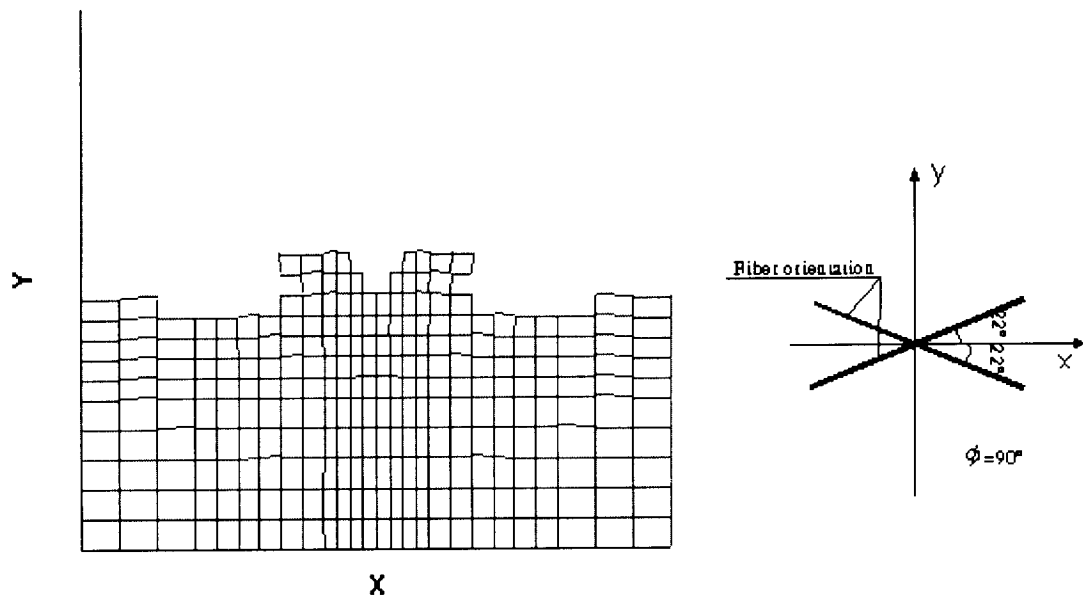


Figure 1.13.5 Final finite element mesh of SS-E specimen

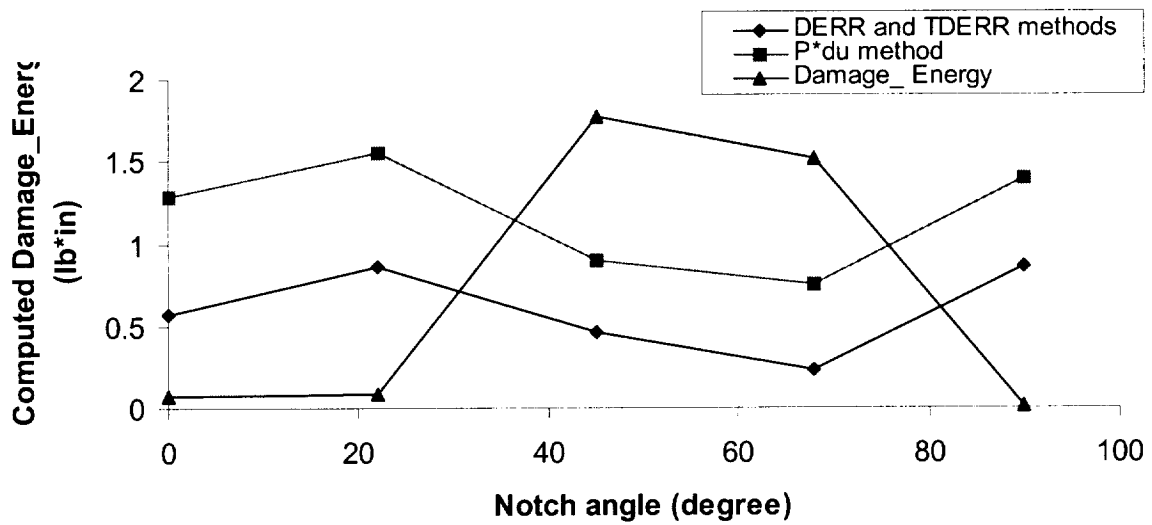
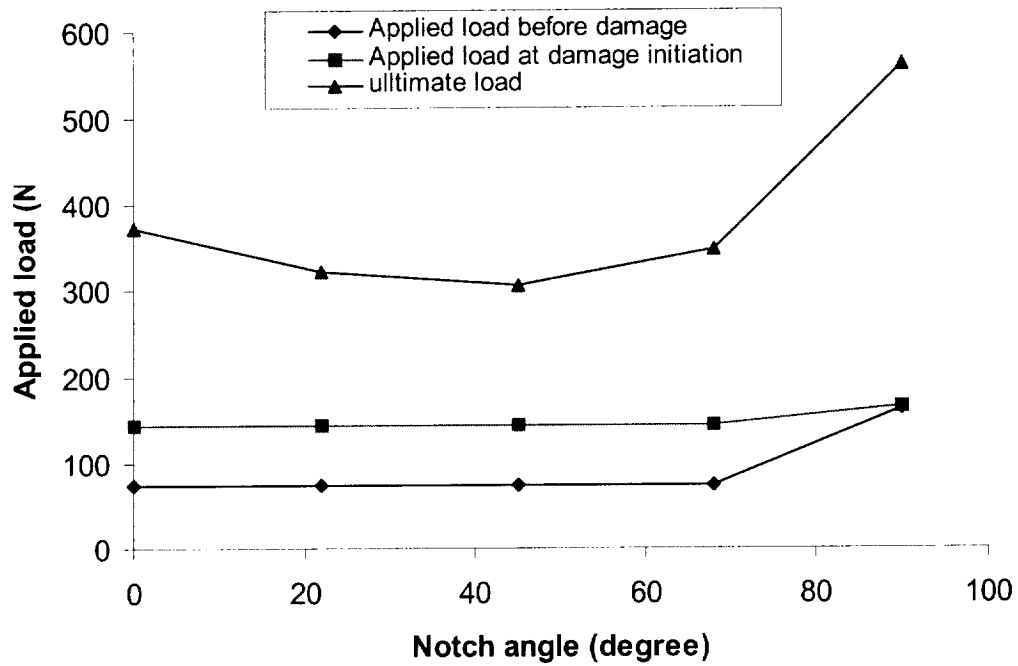


Figure 1.14 Computed Damage\_Energy vs. Notch angle for short sharp notched specimens



**Figure 1.15 Applied load in different stages vs. notch angle for short blunt notched specimens**

## **Chapter II. State-of-the-art of fiber-optic sensor systems in composite structures**

Fracture toughness parameters evaluated via computational simulation need be validated by test data. In particular, built-in strain sensors such as fiber-optic systems that evaluate local deformations are essential for detection of in-service damage initiation and propagation as well as the experimental characterization of fracture toughness and composite structural damage. In general, the presence of fiber-optic sensors would also modify the fracture toughness response of composites. In this chapter a review of the literature is carried out to evaluate the use of fiber-optic sensor systems in composite structures and to assess the potential for applicability of computational simulation to such composites that contain relatively large diameter optical sensor fibers.

### **2.1 Introduction**

Composite materials have been used widely in aerospace, aircraft and automobile industries due to their higher strength, lower weight and other advanced mechanical properties over traditional materials. The stress and strain states of such composite structures while in-service have been one of the major focuses by recent researchers since instant stress/strain extension, instant damage information and fatigue damage detection abilities will help fulfill the structure rehabilitation and life estimation. Traditional methods like electronic strain gauge, infrared, ultrasonic and frequency inspection methods can measure the strain/displacements of structures/components. However, the results are disturbed by the surrounding environments like the temperature elevation, chemical exposure, electromagnetic induction, etc. Since the first use of optical fibers in the telecommunications industry in the mid 1960's, such a technique was developed substantially in the strain measurement and damage detection fields. Based on the fundamental optical principle that the phase, intensity, or wavelength of light waves would be perturbed by the external strain, pressure, or temperature variation, appropriate

methods can be used to analyze the change of one or more of the properties of the light and then relate to the parameters being measured.

In the present chapter, existing research on fiber-optic sensor system are reviewed. Section 2 outlined the fiber optic sensor system and compares it with other traditional structure inspection methods. It is concluded that the embedment of optical fibers influences composite properties. Section 3 introduces the application of fiber optic sensor system in the measurement of strain/stress state of composite structures/components, as well as damage detection and tracking of structural behavior under fatigue loading. Section 4 outlines the previous research of fiber optic sensor system and indicates the inadequateness. Suggestions are outlined to solve the shortcomings in experimental tests. Also computational simulation methods are introduced to help solve the problems that occur in the field of fiber optic sensor system.

## **2.2 Fiber-optic sensors**

### **2.2.1. Advantages over traditional NDI sensors**

Fiber optic sensors as a new method to measure strain, pressure, and environmental variations have anticipated advantages over other traditional non-destructive inspection (NDI) methods by experimental tests and real-time applications. Besides the similar functions as other sensor systems in continuous monitoring of loads and deformations imposed on the materials, fiber optic sensors have the following additional characteristics that are attractive to engineers in the composite structure applications: (1) Typical optical fibers have relatively small size in the order of micrometers ( $\leq 250\mu\text{m}$ ); (2) Embedding ability of fiber optic sensors makes it possible to monitor the internal stress/strain states of the composite specimens/component; if combined with the surface bonding measurement, the structural displacement and strain states can be fully described instantly. (3) Various configurations of fiber-optic sensors provide extensive choices for different usage like localized strain sensing, long-gage strain sensing and strain distribution. Multiplexing capability and distributed sensing system of fiber optic sensors

are useful in large structures to monitor multi-point strain information along the entire length of the fiber. (4) An attractive characteristic of the fiber-optic sensor is that they can work normally and accurately under the harsh environmental conditions like the strong electromagnetic, high temperature, corrosive chemicals, etc. where the traditional electronic strain gages always fail to measure the strain. (5) Long distance data transmission based on the light transmission makes it possible to continuously monitor the health of the structure in service. The distance between the structure and the data conversion instruments can be up to miles away. Such a technique has been used in the transportation fields to monitor the real-time strain and displacement of in-service bridge structures. (6) The good compatibility between optical fibers and the host composite materials guarantees the high accuracy of the measurement results since the spectral content is an intrinsic property of the optical fibers. Previous research on the surface bonding and embedding techniques of the fiber-optic sensors into the composite specimens and structures qualified the adherent compatibility. (7) Extended usage for the fiber-optic sensors is to detect the internal weakness and damage initiation in the structure; this information will help analyze the composite damage process and evolve an optimal composite structure design, as well as fatigue damage detection and life-time estimation. (8) Recalibration is unnecessary as a fiber-optic sensor system keeps its the accuracy in long-term usage.

### **2.2.2. Categories of fiber-optic sensor system**

Categories of fiber-optic sensor systems vary according to different classification criteria. Depending on the optical fiber diameter and the refractive indices of the core and cladding, optical fiber may carry only one (single-mode), or many modes (multi-mode) of the light wave.

According to the transmission mechanism, fiber-optic sensors can be classified as intensity-type sensors, spectrometric sensors and phase sensors. Ansari [1] specified the differences between these three types of sensor systems. Intensity-type sensors based on the intensity modulation analyze the light intensity loses due to the applied strain variation. Spectrometric sensors are based on the wavelength shift due to the strain. Bragg grating technique is applied to form the generally-used spectrometric sensor —



fiber-optic bragg grating (FBG) sensor. Phase sensors can be specified into many types of configurations. One of these types measures the change in the phase of light called interferometric sensor. Michelson scheme interferometric sensors and Mach Zehnder scheme interferometric sensors need the interference of light from two identical single-mode fibers. Fabry-Perot sensor is an advanced example of interferometric sensor that only requires one fiber transmission. Another one takes advantage of the polarization characteristics of light for transmission called polarimetric sensor. Fringe shifts due to the external perturbation like the strain are caused by the interference of two mutually perpendicular polarized waves. Comparing these three types of sensors, intensity-type sensor is simple to measure the localized strain and easy to analyze, but is less sensitive to strain changes. FBG sensors using spectrometric technique are highly intricate but provide sensitivity and reliability. Polarimetric sensors are simple as intensity-type sensors to use only one fiber transmission, but provide the same sensitivity as the interferometric sensors.

Based on the application objectives, the fiber-optic sensors can be divided into strain sensor and stress sensor. Most of the above sensor systems measure the point-like strain or localized strain; a number of researchers have developed multiplexed sensors and distributed sensors based on different transmission mechanisms to record the structural strain variation along the whole fiber. A special fiber optic probe using laser Raman method was introduced by Arjyal et al. [2] to measure the stress distribution directly.

### **2.2.3. General concerns on the fiber optic sensors**

Research on fiber optic sensors has developed for several decades. Experimental tests and in-situ applications demonstrated the feasibility of using fiber-optic sensors in the health monitoring of composite structures and components. Concluding the works by the previous researchers, the major concerns on the application of optical fiber sensors concentrated on the fiber-optic sensor installation, survivability during curing process, effects on material properties by the embedment of fiber optic sensors, and the availability in strain/stress measurement under different loading conditions. Recently, researchers also developed the fiber-optic sensor in the damage detection and in-service

fatigue behavior monitoring. The composite configurations of host materials in the research also extend from the laminated plates to 3D textile materials.

#### 2.2.4. Installation of fiber-optic sensors

Most of literature documentations ignored the installation discussion about the fiber-optic sensor system. As a matter of fact, the good compatibility and stable attachment in the sensor system play very significant roles in the strain and deformation measurement. The interface strain/stress state between the optical fiber and host material directly influence the results. Difference in installation between the calibration process and the application would cause a wrong analysis of the optical information.

The locations of optical fibers have two major types: surface bonding and embedment into the specimen. The difficulties to install the optical fibers are directly related to the small diameter and brittleness of the optical fibers and their circular cross-section that generally cannot match the surface of the specimen. Tatti et al. [3] examined the Michelson scheme interferometric sensor installation in detail. An improved surface bonded fiber-optic sensor system uses grooves under the optical fibers (**Figure 2.1b**) instead of the traditional surface bonding (**Figure 2.1a**). The directions of grooves are controlled crucially to match the mutual orientations of optical fibers, and the dimensions are etched less than the diameter of the optical fibers to avoid their sinking. Such a configuration avoids the above difficulties of traditional bonding methods in the accurate measurement of strain. Results of aluminum cantilever tests with the improved bonding fiber-optic sensor system showed a good agreement with the results from semiconductor electronic strain gauge and beam theory analysis (**Figure 2.2**).

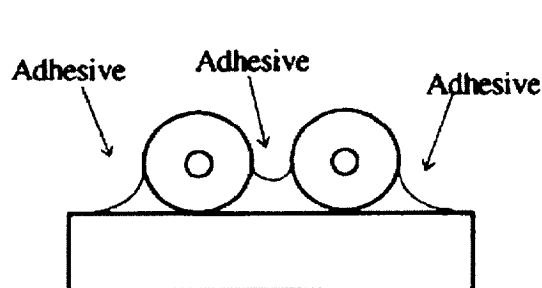


**Figure 2.1(a). Original optical fiber bonding**

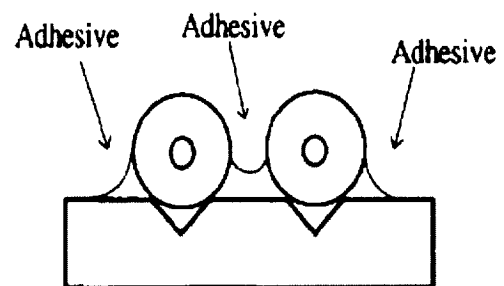


**Figure 2.1(b). Improved optical fiber bonding**

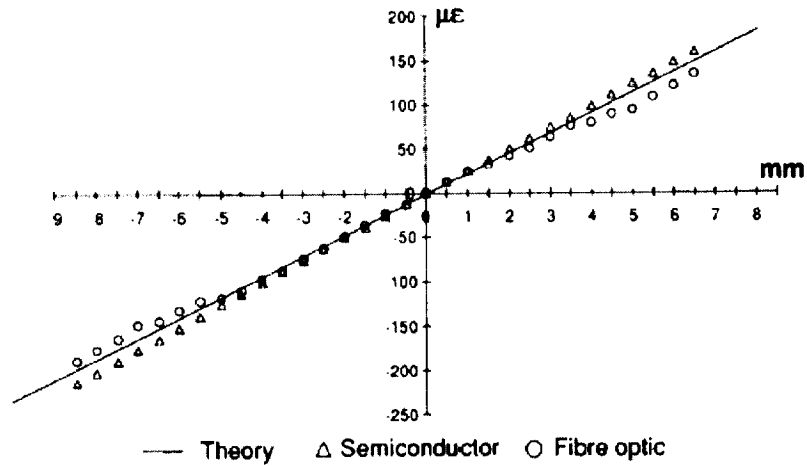


**Figure 2.2. Comparison of different methods of edge section displacement in the aluminum cantilever beam test**

One difficulty in the installation of embedded fiber-optical sensor system happens mainly in the aircraft composite components edge connections. The major concerns focus on the ingress/egress damage of the optical fibers, inconvenient in the edge trimming by the exit of the embedded optical fibers during fabrication and optic loss by the fiber connections. Sjogren [4] developed polytetrafluoroethylene (PTFE) dummies in the manufacturing and solved the laminate component edge trim problem. In this method, laminates were manufactured with embedded fiber optic connections like MT-ferrules and FC-ferrules. The dummies could easily be removed after the curing of laminates and edge trimming, leaving embedded ferrules at the laminate edges, ready for connection of mating ferrules. The optic losses in the fiber-optic connections were also measured by the use of power meter and found to be generally 1.5dB[5]. Following sections will mainly discuss embedded fiber-optic sensors.

#### **2.2.5. Survivability in curing process and fabricating process**

Composite curing processes always experience the change of temperature, chemical process, and loading conditions. The survivability of embedded fiber-optic sensor under high curing temperature and chemical reaction requires proper selection of fiber coatings

and different sensors. According to present literature, two types of the fiber coatings dominate the research field about the interface effects on composite mechanical properties. One is the polyimide coating, and the other is acrylate coating. Kalamkarov et al. [6] investigated the different effects of these two types of coatings on FBG sensors during the pultruded curing process. Experiments showed that Polyimide coating on the optical fiber resulted in good bond at high production temperature (up to 385°C), but the acrylate coating debonded in a harsh production process where the temperature was higher than 85°C, which was reported as the greatest survival temperature for acrylate coating. Weak bond by acrylate coatings with concrete was also achieved when the fiber-optic sensors were embedded in the cementitious materials [7]. Other discussions also were found in [8-10]. FBG shows greater survivability than the FP sensor [11].

#### **2.2.6. Effects of embedded fiber optic sensor on material properties**

Effects on composite material properties by embedment of fiber-optic sensors have been investigated by previous researchers. Most of the concerns are structural strength loss during curing process and under different loading conditions since the stress and strain concentrations may be induced. A few tests were also conducted to determine the modulus changes by the embedded sensors. Besides the different loading conditions, the effects of the embedded fiber-optic sensors on the change of composite mechanical properties also depended on other factors, such as optical fiber coating types, optical fiber embedment location and fiber-optic sensor types, etc.

##### ***2.2.6.1. Coating types effects***

Strain transferring from matrix to an embedded optical fiber directly determines the accuracy of the measurement and depends on the coating types. All the discussions about the effects of embedment of fiber-optic sensor on the properties change rely on the survivability of the coating materials, which was discussed above. Previous research showed that polyimide coatings around optic fibers have more ability to survive under harsh environmental conditions than the acrylate coatings.

#### ***2.2.6.2. Embedment location and direction***

In order to have reliable internal strain of composite materials from embedded sensor system, the exact location must be obtained. Bosia et al [12] divided the embedment locations into three cases in a cross ply laminate: (1) between two 0 layers and the optical fiber parallel to the reinforcement fiber without perturbing the interface; (2) between a 0 layer and a non-0 layer, the optical fiber tries to position itself in 0 layer; (3) between two non-0 layers, a local perturbation occurs. Experimental results revealed that different locations of sensors only measured the local strain states. In order to evaluate whole structural strain variation, correct location of sensors need to be indicated and a proper factor needs to be specified to calculate the overall strain state. Investigations by Surgeon et al. [13] showed that the different embedment locations and directions of optical fibers caused great changes of the structural strength in bending tests and showed little effects in the tension tests.

#### ***2.2.6.3. Strength loss by embedded fiber-optic sensors***

Arjyal et al [2] discussed that optical sensor embedment parallel and perpendicular to the reinforcing fibers caused different effects on the structural strength reduction. Results showed the perpendicular configuration was found to reduce the tensile strength of the non-embedment composite coupon by 10% whereas the parallel second configuration had no effect.

Sjogren [5] developed PTFE to solve the edge trimming and connecting problems and discovered the edge connector embedment resulted in a significant reduction of both the tensile and compressive strength of composite specimens due to the extensive ply waviness. Results revealed that the tensile failure stress and strain reduction was less notable and limited to about 25% if bigger specimen was used. However, the size effect on compressive failure and fatigue damage with embedment of fiber-optic ferrules were not involved due to a lack of anti-buckling guides. Future work needs to be concerned with the local buckling issue.

Kalamkarov et al [6] examined effects of embedded fiber-optic sensors on the composite strength under pultrusion tests. Experimental results showed that embedded

optical fibers influenced the tensile properties less in the fiber directions for unidirectional composite and can be neglected (**Figure 2.3**), but greater influence on the shear strength was shown (**Figure 2.4**). The diagram also indicated that the embedded optical fibers cause more reduction of shear strength in GFRP than CFRP.

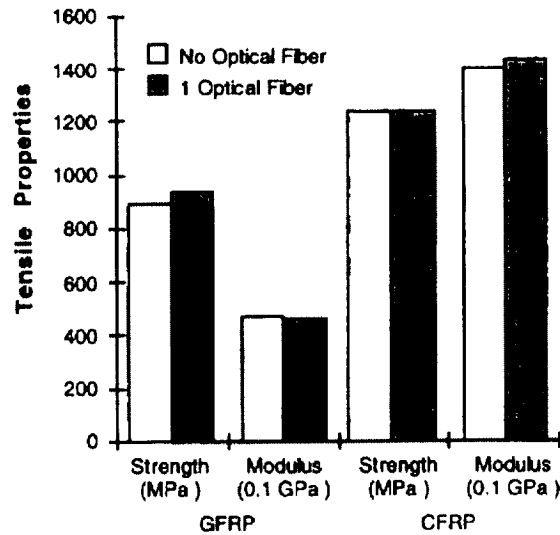


**Figure 2.3. Comparison of tensile properties of pultruded CFRP and GFRP**

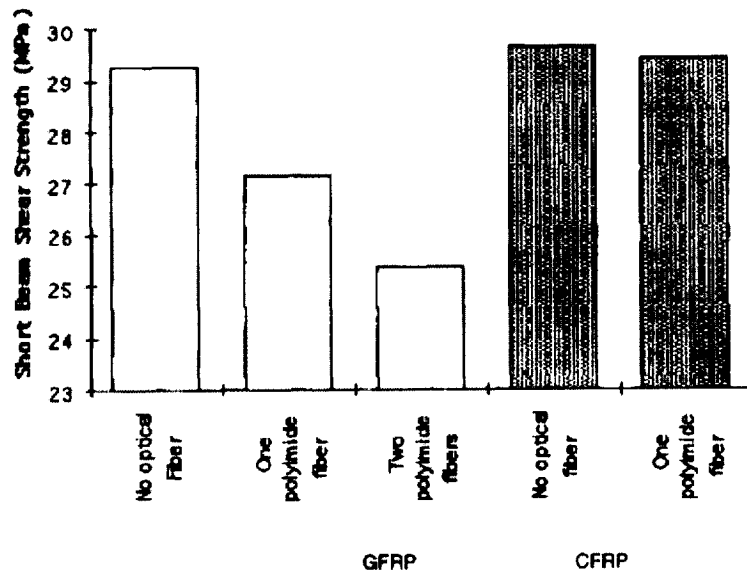


**Figure 2.4. Comparison of shear properties of pultruded CFRP and GFRP**

Bosia et al [12] obtained the results of effects on global mechanical properties by embedded fiber-optic sensors from three-point bending tests. Eight-ply composites with up to two embedded FBG sensors were examined. Load-deflection curves revealed that the embedded two or less fiber-optic sensors caused less than 5% difference in global flexural mechanical properties in the three-point bending tests. Surgeon et al.[13] also examined the strength of quasi-isotropic laminates [0/45/-45/90]s under three-point bending and four-point bending tests with two embedded fiber-optic sensors in different layers. The different embedment locations caused obviously different reductions of the bending strength.

## **2.3 Applications of fiber-optic sensors**

### **2.3.1. Strain measurement**

Arjyal et al. [2] tested unidirectional Kevlar 49®/Epoxy composite and multidirectional laminates [0<sub>2</sub>/-45/45]s under tension-tension loading condition till the structural failure of specimens. A remote laser Raman microprobe (ReRaM) sensor system was applied to measure the bulk and surface strain/stress of the specimens. Optical fibers were embedded parallel or perpendicular to the reinforcement fibers. Results provided information about the effects by different embedment of optical fibers on material strength as was discussed above. Tensile strains measured by both parallel and perpendicular ReRaM sensor system in unidirectional laminates showed linear relationship with the measured strain by electronic strain gauges, which indicated the applicability in the strain measurement by ReRaM sensor system on unidirectional laminates. Stresses measured by ReRaM sensor in multidirectional laminates clearly described the stress distribution in different fiber plies. Results in **Figure 2.5** indicate that with the increase of applied tensile stresses, the 0° plies endure most of the stresses, whereas the principal stresses in the 45° plies contribute only a small fraction.

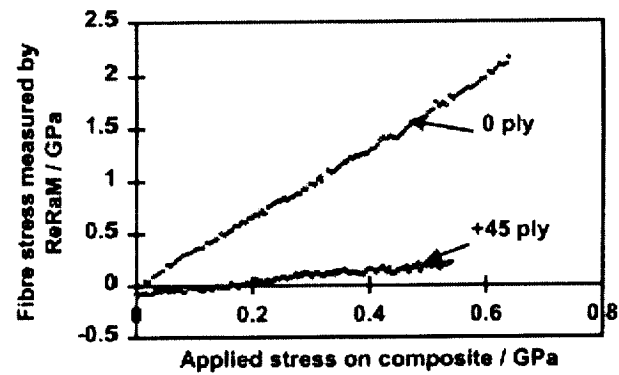


**Figure 2.5. Stress distributions in 0° and 45° ply of [0<sub>2</sub>, -45, +45]<sub>s</sub> multiply laminate under tension tests.**

Bosia et al. [12] measured through-the-thickness strain of 8-ply and 16-ply laminated plates with cross-ply configurations using combined embedded FBG sensors and ESPI (electronic speckle pattern interferometry) sensor system in simply supported three-point bending tests. Results showed detailed strain distribution of laminates through the whole thickness under flexural tests in **Figure 2.6**. 8-ply laminates displayed linear relationship of strain through the thickness, whereas the 16-ply laminates expressed non-linearity in the strains since the thickness of 10 mm fell in the “thick-plate” range [14]. ESPI sensor was also used to measure out-of-plane deformations and provided adequate information to model the mechanical behavior of the laminated plates. Such information can be used as a demonstration to evaluate the existing theory on the analysis of laminated composite properties and behaviors [14].



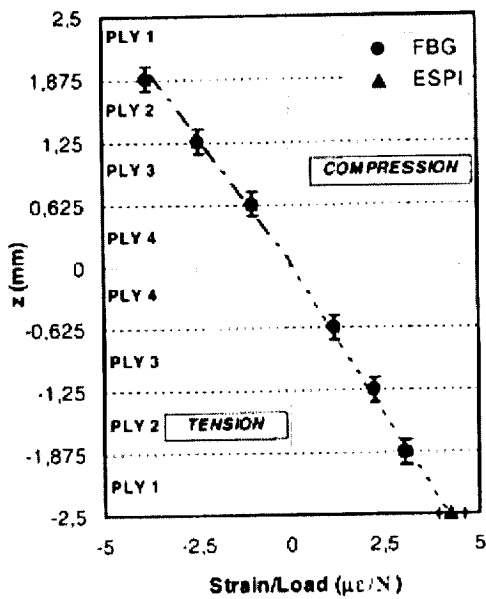


**Figure 2.6a. Through- the-thickness strain distribution per unit loading in 8-ply laminate**

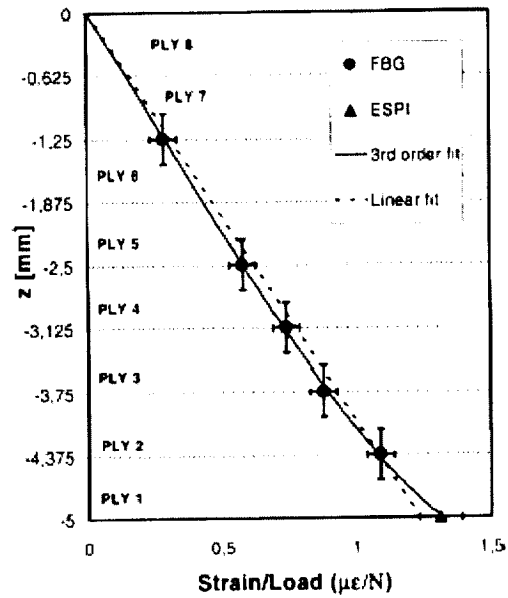


**Figure 2.6b. Through- the-thickness strain distribution per unit loading in 16-ply laminate**

Melin et al [15] concluded that the embedment of fiber-optic sensor in the composite materials caused large strain gradients around the embedded optical fibers. Experimental specimen was a unidirectional laminated plate under compression loading tests (**Figure 2.7**). An interferometry sensor system recorded the displacement field around optical fiber during different loading stages. **Figure 2.8** showed the strain gradients around the optical fiber under 1.0KN and 2.0KN loads on the side surface. There was obvious strain concentration around optical fiber, however the influence decreased quickly. At a distance more than 0.1mm stress concentrations would have no influence. Average strain in loading direction showed nearly linear relationship with global stress in **Figure 2.9** except the area around fiber-optic sensor (less than 0.1mm).

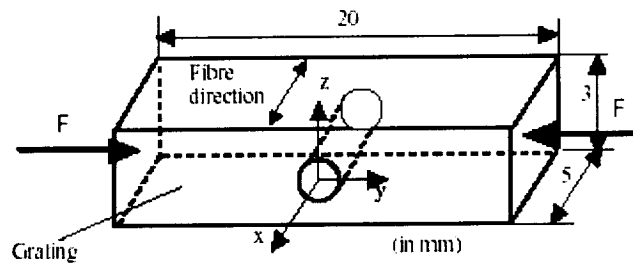


**Figure 2.7. Compressive specimen with central embedded optic fiber.**

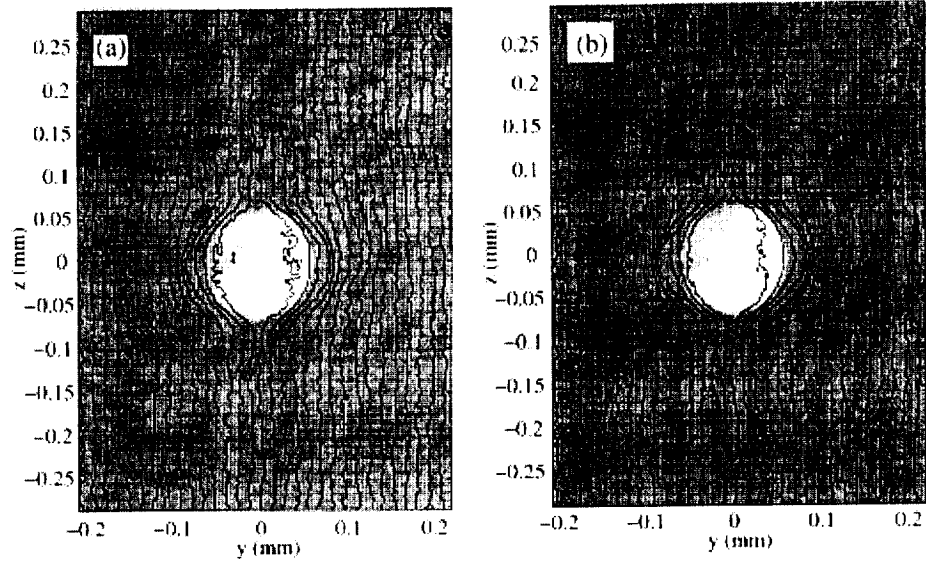


Figure 2.8. (a) 1.0 kN load, contour interval 0.1  $\mu\text{m}$ ;  
(b) 2.0 kN load, contour interval 0.2  $\mu\text{m}$ .

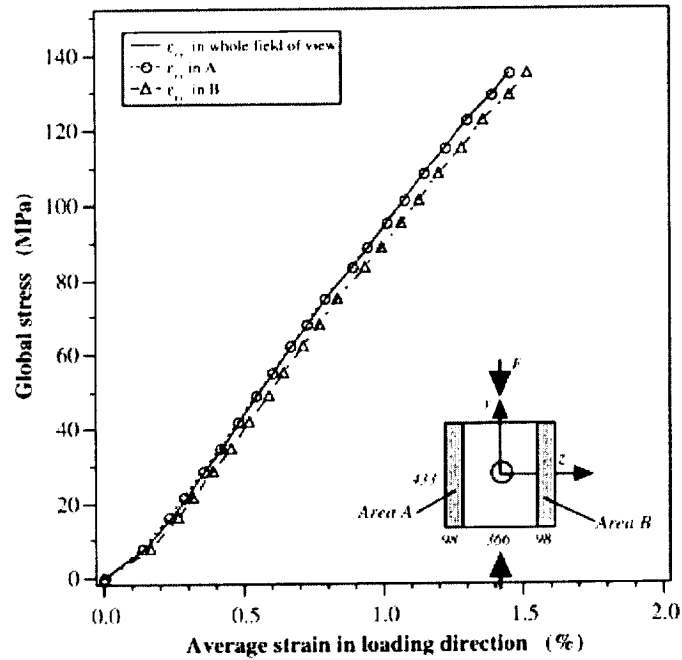


Figure 2.9. Global stress vs. average strain curve.

Sensitivity and accuracy of strain measurement using different fiber-optic sensing system depend on the parameters of the sensors. Murukeshan et al. [16] studied the effects of various parameters such as the pre-stress, input azimuth, light types in fiber,

fiber-coating and fiber types on the polarimetric fiber optic sensing system for CFRP and GFRP laminates in three-point or four-point bending tests. Such investigations demonstrated the importance of using the same parameters in real application and calculation of fiber-optic sensing system.

### **2.3.2. Damage detection**

Fiber-optic sensor system has ability to measure the strain of composite material under different loading and environmental conditions. This has been demonstrated by amounts of experiments and research. Structural rehabilitation and maintenance are important to keep normal function of composite structures. The failure process and damage detection of composite structures are also important issues in real application of fiber-optic sensors.

Kwon et al. [17] used fiber-optic Michelson sensor system to measure internal strain of composite laminate and to monitor the points of damage simultaneously. Graphite/Epoxy laminated plates with cross-ply stacking configuration  $[90_4/0_4]_s$  were tested under four-point bending loading condition. Interferometric sensors of Michelson type were embedded inside the cross-ply composite beams and distributed in the tension and compression zones and neutral planes, and PZT sensors were bonded on the top of specimens. A method was introduced to convert the digital signal to strain measurement. Low- and high-pass filtering found the strain process and instant failure by the optical signals respectively. Fiber-optic sensor signals were compared with PZT sensor to confirm the failure detection (**Figure 2.10**). Comparing the results of embedded fiber-optic sensors in the tension region and compression region with the PZT top surface sensor showed good agreement for the instant failure detection by the sudden change in the response signals. Results also revealed that the embedment location of the optical fiber did not affect the fiber optic failure signal.

### **2.3.3. Fatigue problems**

Fiber-optic sensor system can also be used in the strain measurement under fatigue loading conditions. Kalamkarov et al. [11] examined performance of fiber-optic sensors in the composite rod under trapezoidal quasi-static and sinusoidal cyclic loading.

Microstrain obtained from FBG sensor and Fabry-Perot sensor were compared with the surface-bonded extensometer. As an example, results of microstrain versus sinusoidal load in **Figure 2.11** showed good agreements between optic sensors and extensometer. In addition to this, profiles of microstrain versus time (**Figure 2.12**) matched the different loading stages. Kalamkarov et al. [18] also demonstrated the feasibility of strain measurement by Fabry-Perot sensors in CFRP and GFRP rods during pultrusion tests under fatigue loading with temperature range from  $-40^{\circ}\text{C}$  to  $60^{\circ}\text{C}$ .

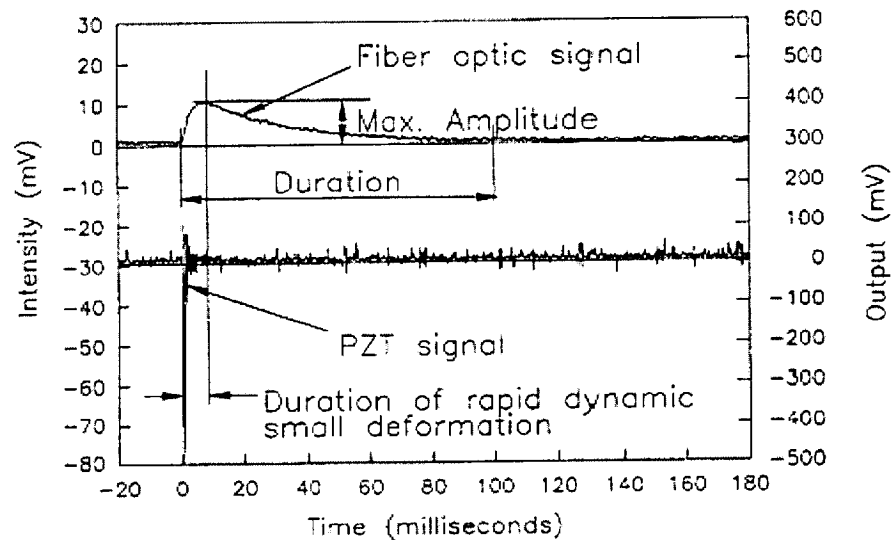


**Figure 2.10. Comparison of the fiber optic failure signal with PZT signal for a  $[90_4/0_4]_s$**

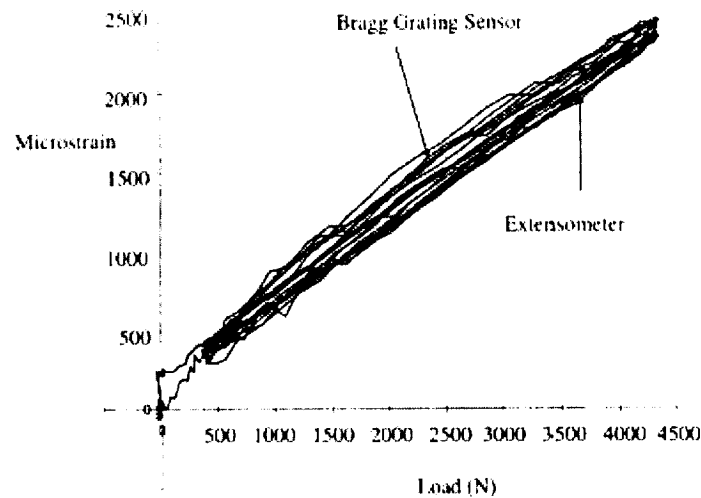


**Figure 2.11. Strain from extensometer and embedded Bragg Grating sensor in a FRP tendon subjected to a sinusoidal load**

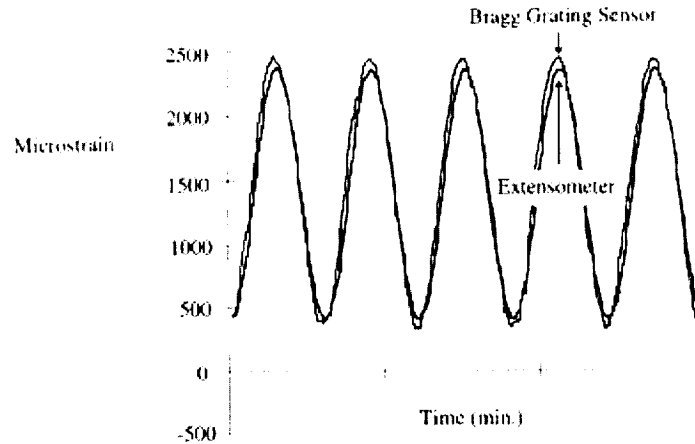


**Figure 2.12. Strain vs. time plot from extensometer and Bragg Grating sensor in a glass tendon subjected to a sinusoidal load**

#### 2.3.4. Curing monitoring

It is known that the process of fabricating composite materials experiences temperature change and certain loading stages. Such procedures for many composites inevitably cause residual stresses and strains that may lead to problems such as warping, delamination, and micro-cracks in composite matrix during their applications. Fiber-optic sensors can be used to measure internal strain and temperature. They can also be used in curing process to obtain strain data caused by loading or by thermal expansion or contraction. Experimental results of pultrusion showed that thermal strain obtained from the embedded FBG sensor or Fabry-Perot sensor gave the similar profile as the temperature variation during curing process [19]. Brown et al.[20] also investigated the internal phase chemical reaction of composite specimen during curing process using a Fourier transform near infra-red fiber-optic conversion sensor. Cusano et al.[21] investigated the FOS (fiber optic sensor) during the curing process in thermoset-based polymer-matrix composite. A single mode fiber and an amplitude-modulated source were used in order to monitor the variations of the refractive index due to the curing process of an epoxy-based resin. The authors introduced a calibration method of fiber-optic sensors and proved the validity of the calibration procedure that provided a method for obtaining in-situ measurements of the conversion degree for isothermal cure reactions. Results revealed that increasing the isothermal cure temperature resulted in a higher conversion.

### 2.3.5. Textile material test monitoring

Most of the previous research concerned fiber-optic sensors in laminated plates under different loading states and environmental conditions and obtained dramatic success. With the recognition of the advantages of textile materials over traditional materials such as higher out-of plane stiffness, higher energy absorption, and the absence of delamination, a few investigations were carried out to evaluate the applicability of strain measurement in textile material by embedded fiber-optic sensors. Rao et al. [22] examined the behaviors of two types of fiber-optic sensor system in 3-D braided composite materials under tensile tests and different temperature conditions. An integrated sensing system by FBG sensor and EFPI (extrinsic Fabry-Perot interferometric) sensor system was used to measure the strain by loading and temperature simultaneously. This system sufficiently utilized the high accuracy of FBG sensor to measure the temperature and the ability of EFPI in measuring the strain by loading or by temperature variation. **Figure 2.13** showed good agreement of tensile strain records between EFPI sensor and electronic strain gauge. In order to reduce the effects of the distortion of optical spectrum by the combination of FBG and EFPI sensors on the accuracy in temperature measurement, the authors used the averaged central wavelength of FBG sensor and obtained a static linear relationship between the wavelength and temperature. Such results demonstrated the usability of fiber-optic sensor system in measuring strain and temperature of 3-D braided materials during and after curing process.

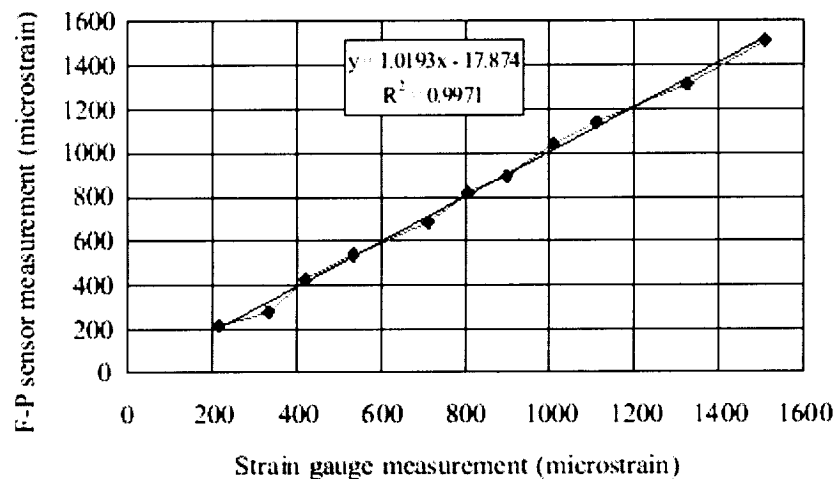


**Figure 2.13. Experimental results for strain measurement**

## 2.4 Summary

Fiber-optic sensors have been studied and successfully used since they were introduced into the civil engineering field. Their advantages over traditional NDI sensor system like small size, immune to harsh environmental conditions, and embedment capability are attractive to researchers and users. Also, various types of fiber-optic sensors provide sufficient selections for users to adapt different measuring requirements. A large number of laboratory tests and industrial applications have been implemented to exploit the usages of fiber-optic sensors and verify their feasibility in measurement of structural health. Considerable results were obtained in strain and deformation measurement by the application of fiber-optic sensor system. Embedment of fiber-optic sensor provides an opportunity to measure the internal strain and relative deformation information. Multiplexed and distributed fiber-optic sensors can be used to measure the strain along the entire optical fiber. However, embedment of fiber-optic sensor causes the stress and strain concentrations resulting in the change of mechanical properties in composite materials. Such a reduction can be estimated and restricted by other factors like size effects. In addition to the fundamental strain measurement, extended usage in damage detection and fatigue process tracking were also found in present documentations. Compared with other traditional damage detection techniques, fiber-optic sensor has the most appealing characteristic of in-service detection capability.

Based on present paper review, although the testing results and research in application of fiber-optic sensor technique have been developed for several decades, additional study and research are still needed. Here, some of the predicted future directions of fiber optic sensing in composites are enumerated:

(1) Size of optical fiber is actually much larger than the reinforcement fibers. Embedment of such fibers into composite unavoidably results in a sudden change in the structural configuration of composite material, especially for non-unidirectional laminates and textile composites, which causes the stress/strain concentration around the optical fibers and the reduction of mechanical properties. Previous research has addressed this shortcoming of fiber-optic sensors and obtained certain results. However, because of different selections in sensor system such as calibration methods and sensor configurations by each researcher, individual results are difficult to be compared to form

a reliable and directly usable module in analyzing the effects of embedded optical fibers and therefore inconvenient for design. General views of previous discussion can only be used as references in real applications. One of the solutions is to standardize configuration of different fiber-optical sensor systems (i.e. detailed parameters of fiber-optical sensor). Material testing based on the same standard may provide useful information in integrate analysis of effects of fiber-optic sensors.

(2) Specimens under tension, compression and flexure loading conditions have been tested with fiber-optic sensors. Strain measurements have shown good agreement with traditional strain gauge bonded on the specimen surfaces and theoretical calculations. Results have proven the validity of fiber optic internal strain measurement. However, most of the test specimens were simple and with no crack initiation. In practice, composite structures with fiber-optic sensor cannot avoid existing flaws and damage initiation in real implementation. Additional material testing of fiber-optic sensor should include pre-cracked specimens such as compact tension specimen, bending beam with pre-crack and tension plane with existing crack.

(3) Previous tests concerned the strain measurement by the fiber-optical sensors during loading application process and neglected the failure analysis. Future work need be done to fulfill this field. For example, delamination is the most prevailing failure mode in laminated plates. Most of the tests were based on the laminated plates and neglected the analysis of detection of delamination by the fiber-optic sensors during loading process.

(4) Some tests included the measurement of strain behaviors under sinusoidal cyclic and trapezoidal quasi-static loading conditions. Results showed that fiber-optic sensor system provided continuous information during fatigue loading process. In particular, research needs about the sensor detection capability of fatigue damage initiation and damage propagation till the structural failure need to be addressed. Future work may focus on the damage initiation detection of fiber-optic sensor system, which is important as an indication for structural rehabilitation and maintenance.

(5) Based on an established standard, more experiments need to analyze the influence of the embedded optical fibers on mechanical properties of composite materials.



Fiber-optic sensor systems achieved great success in laboratory material testing. However, they have experienced limited practical usage for only relatively important components in aircraft structures and some transportation structures. The reason is not only that the technology of fiber-optic sensor system is intricate and has not reached to a state of maturity, but also the testing and implementation of fiber-optic sensors is time consuming and costly. With the development of powerful and sophisticated numerical methods for structural analysis in composite research using computer technology, computational simulation is a useful tool in the material properties analysis. Material tests with embedded fiber-optic sensors also can utilize the advanced computer technology in the following aspects:

(1) As discussed above, the embedment of optical fiber causes the change of material properties. Traditional method follows the process of: fabricating a specimen, embedding fiber-optic sensor, then testing the whole material properties under different loading and environmental conditions. Analysis based on such a process obviously depends on many factors like the installation of fiber-optic sensor, optical fiber embedment location, direction, etc. Also if any one of these factors changes, the tests have to be repeated. Computational simulation can easily solve this problem. Proper theory selection and accurate mechanical analysis can evaluate the effects of embedded optical fiber on material properties quickly and precisely.

(2) Although fiber-optic sensor has a number of advantages over traditional sensor systems, the most important one is damage detection of composite structure during service. Localized fiber-optic sensor or multiplex/distributed fiber-optic sensor system can only monitor the damage initiation and progression where the sensor was embedded. To solve this problem, predicting positions of weakness in the composite structures is required before embedding sensor system. Computational simulation can provide weakness positions of composite structure and information of damage like position, value and reason. Analysis by simulation helps correct and renders more effective embedment of fiber-optic sensor system.

(3) In-service structure with embedded fiber-optic sensor system can indicate the damage initiation information and send out structural maintenance signal. Computational

simulation of composite structure with damage initiation detected by embedded fiber-optic sensor can help decide detailed information of damage propagation and serious degree. A more reliable suggestion of rehabilitation and maintenance can be made based on simulation analysis.

## **2.5 Conclusion**

Fiber-optic sensor system shows advantages in health monitoring of composite material than the traditional NDI methods under severe conditions. Considerable laboratory tests and engineering applications proved the feasibility of fiber-optic sensor system in the strain measurement, damage detection, curing monitoring and fatigue damage tracking in-service. However, just as indicated in previous section, both the experimental tests and on-site applications of fiber-optic sensor system met with the lack of standard and need more tests to solve the shortcomings. Computational simulation is one of new methods to develop the fiber-optic sensor system. Pre-analysis of stress/strain states in composite structures can help predict the influence of embedded optic fiber on the structural mechanics and suggest optimal design of fiber-optic sensor system. In Chapter III we will discuss the computational method and the simulation of several coupons to compare with the experimental tests.

## **2.6 References for Chapter II**

1. Farhad Ansari, "State-of-the-art in the Applications of Fiber-optic Sensors to Cementitious Composites," *Cement and Concrete Composites*, Volume 19, Issue 1, 1997, Pages 3-19.
2. B. P. Arjyal, P. A. Tarantili, A. G. Andreopoulos and C. Galiotis, "Surface and bulk stress/strain measurements in composite laminates with a fibre-optic Raman

- probe,” *Composites Part A: Applied Science and Manufacturing*, Volume 30, Issue 10, October 1999, Pages 1187-1195.
3. M. Tatti, G. Sala and P. Mantegazza, “Production and Use of an Interferometric Optic Stain Gauge with Comparison to Conventional Techniques,” *Optics and Lasers in Engineering*, v. 27, pp.269-284, 1997.
  4. B. A. Sjögren, “Manufacturing technique for embedding detachable fiber-optic connections in aircraft composite components”, *Smart mater. Struct.* 2000, vol. 9, pp855-858.
  5. B. A. Sjögren, “Static strength of CFRP laminates with embedded fiber-optic edge connectors,” *Composites Part A: Applied Science and Manufacturing*, Volume 32, Issue 2, February 2001, Pages 189-196.
  6. A. L. Kalamkarov, H. Q. Liu and D. O. MacDonald, “Experimental and analytical studies of smart composite reinforcement,” *Composites Part B: Engineering*, Volume 29, Issue 1, 1998, Pages 21-30
  7. Christopher K. Y. Leung, Niell Elvin, Noah Olson, Theodore F. Morse and Yi-Fei He, “A novel distributed optical crack sensor for concrete structures,” *Engineering Fracture Mechanics*, Volume 65, Issues 2-3, 1 January 2000, Pages 133-148
  8. Qingbin Li, Libo Yuan and Farhad Ansari, “Model for measurement of thermal expansion coefficient of concrete by fiber optic sensor,” *International Journal of Solids and Structures*, *In Press, Uncorrected Proof*, Available online 8 May 2002.
  9. Qingbin Li and Farhad Ansari, “Circumferential strain measurement of high strength concrete in triaxial compression by fiber optic sensor,” *International Journal of Solids and Structures*, Volume 38, Issues 42-43, October 2001, Pages 7607-7625
  10. W. R. Habel, D. Hofmann and B. Hillemeier, “Deformation Measurements of Mortars at Early Ages and of Large Concrete Components on Site by Means of Embedded Fiber-optic Microstrain Sensors,” *Cement and Concrete Composites*, Volume 19, Issue 1, 1997, Pages 81-102
  11. A. L. Kalamkarov, S. B. Fitzgerald, D. O. MacDonald and A. V. Georgiades, “On the processing and evaluation of pultruded smart composites,” *Composites Part B: Engineering*, Volume 30, Issue 7, October 1999, Pages 753-763
  12. Federico Bosia, John Botsis, Mauro Facchini and Philippe Giaccari, “Deformation characteristics of composite laminates—part I: speckle interferometry and embedded Bragg grating sensor measurements,” *Composites Science and Technology*, Volume 62, Issue 1, January 2002, Pages 41-54
  13. M. Surgeon and M. Wevers, “Static and dynamic testing of a quasi-isotropic composite with embedded optical fibres,” *Composites Part A: Applied Science and Manufacturing*, Volume 30, Issue 3, March 1999, Pages 317-324
  14. Federico Bosia, John Botsis, Mauro Facchini and Philippe Giaccari, “Deformation characteristics of composite laminates—part II: an experimental/numerical study on equivalent single-layer theories,” *Composites Science and Technology*, Volume 62, Issue 1, January 2002, Pages 55-66
  15. L. G. Melin, K. Levin, S. Nilsson, S. J. P. Palmer and P. Rae, “A study of the displacement field around embedded fibre optic sensors,” *Composites Part A:*

- Applied Science and Manufacturing*, Volume 30, Issue 11, November 1999, Pages 1267-1275
16. V. M. Murukeshan, P. Y. Chan, L. S. Ong and A. Asundi, "Effects of different parameters on the performance of a fiber polarimetric sensor for smart structure applications," *Sensors and Actuators: A Physical Volume 80*, Issue 3, March 2000, Pages 249-255
  17. I. B. Kwon, C. G. Kim and C. S. Hong, "Simultaneous sensing of the strain and points of failure in composite beams with an embedded fiber optic Michelson sensor," *Composites Science and Technology*, Volume 57, Issue 12, 16 January 1998, Pages 1639-1651
  18. Alexander L. Kalamkarov, Stephen B. Fitzgerald, Douglas O. MacDonald and Anastasis V. Georgiades, "The mechanical performance of pultruded composite rods with embedded fiber-optic sensors," *Composites Science and Technology*, Volume 60, Issue 8, June 2000, Pages 1161-1169
  19. A. L. Kalamkarov, S. B. Fitzgerald and D. O. MacDonald, "**The use of Fabry Perot fiber optic sensors to monitor residual strains during pultrusion of FRP composites,**" *Composites Part B: Engineering*, Volume 30, Issue 2, March 1999, Pages 167-175
  20. J. M. Brown, S. Srinivasan, A. Rau, T. C. Ward, J. E. McGrath, A. C. Loos, D. Hood, D. E. Kranbeuhl, "**Production of controlled networks and morphologies in toughened thermosetting resins using real-time, in situ cure monitoring,**" *Polymer*, Volume 37, Issue 9, April 1996, Pages 1691-1696
  21. Andrea Cusano, Giovanni Breglio, Michele Giordano, Antonio Calabrò, Antonello Cutolo and Luigi Nicolais, "**An optoelectronic sensor for cure monitoring in thermoset-based composites,**" *Sensors and Actuators: A Physical*, Volume 84, Issue 3, September 2000, Pages 270-275
  22. Y.J. Rao et al., "**Simutaneous strain and temperature measurement of advanced 3-D braided composite materials using an improved EFPI/FBG system,**" *Optics and Lasers in Engineering*, accepted 7 January 2002, *In Press, Uncorrected Proof*,

## **Chapter III. Fiber optic sensor system in composite structures: computational simulation of damage propagation with embedded fiber-optic sensors**

In this chapter fracture toughness evaluation via computational simulation is extended to composite structures containing irregular fiber patterns such as a fiber optic sensor that may be embedded in a graphite/epoxy fiber composite structure to detect load induced damage during service. Embedded sensors to detect damage are an essential part of reliable aeronautical and space structures. Therefore the fracture toughness of composites with embedded sensors is of significant interest to the aerospace engineering community. Damage progression characteristics as well as the ultimate structural fracture loads are computed and compared with test data. The effects of sensor fiber orientation with reference to the composite structural fiber orientation and loading are examined with respect to their influences on damage and fracture progression characteristics. Fracture modes associated with the microscopic subply stresses due to the different fiber orientation and specimen dimensions are identified. Results validate the computational simulation method and identify the damage initiation, growth, accumulation, and progressive fracture stages for composites with embedded sensor fibers.

### **3.1 Introduction**

Fiber-optic sensor system is one of the best methods of on-site structural health monitoring and enjoys numerous advantages over traditional sensor systems, especially under harsh environmental conditions like the strong electromagnetic, high temperature and corrosive chemicals. Embedment capability of optical fiber helps measure the strain/stress status and detect the damage points in structure during service. However, use of embedded optical fibers may have adverse influences on physical and mechanical properties of the master composite structure. Prediction of the changes in structural properties and measurement accuracy has been the major concern of previous research on fiber-optic sensor system.

Computational simulation is used in the evaluation of composite material properties and failure behavior of structures/components. Previous research on simulation of composite structures proved the feasibility of predicting the micro- and macro-level mechanics of different composite specimens, as well as the description of the damage progression [2-9]. Compared with traditional testing methods, computer based methods solve the shortcomings of time consuming and high cost due to laboratory or on-site tests. Moreover, the capability to adjust computational scales according to the needed accuracy makes simulation more attractive in the evaluation of structures under various loading and environmental conditions.

Present research introduces the computational method into the application of fiber-optic sensor system to predict the effects of embedded optical fibers on the mechanical properties and describe the damage progression of different specimens with embedded optical fibers. In this report, the methodology of CODSTRAN computer code was extended to model specimens with different configurations of fiber-optic sensor embedment. The parallel and perpendicular configuration of optical fibers embedded in unidirectional laminates was examined under uniaxial tension tests. Micro-damage progression under increasing loading was described by simulation results. Ultimate strength and stress distribution in each layer obtained from simulation were compared with physical test results. Reduction of mechanical properties due to embedment of optical fiber was analyzed.

### **3.2 Methodology**

The integrated stand-alone computer code CODSTRAN [10] used in this report comprises three modules: composite mechanics module (ICAN), structural analysis module (MHOST), and damage progression module. The damage progression module keeps a detailed account of composite degradation for the entire structure. It also acts as the master executive module that directs a composite mechanics code (Murthy and Chamis 1986) [11] to perform micromechanics and macromechanics analysis/synthesis

functions, and calls the structural analysis module with finite element analysis capability [12] to model composites for global structural response.

Prior to each finite element analysis, the composite mechanics module utilizes a resident databank that contains the typical fiber and matrix constituent properties and computes the composite properties. After each finite element analysis, it helps determine whether or not the structure in its current state is in equilibrium under the applied loading and also helps evaluate the ability of composite structure to endure stresses and deformations due to additional loading increments. Composite properties are computed from the properties of fiber and matrix, based on the intraply composite micromechanics theory (Chamis and Sinclair, 1979) [13] for each subvolume and average stiffness method for computation of ply properties.

Although anisotropic three-dimensional solid elements can accept the 3-D composite properties directly, the resulting computational model requires huge computer resources and is usually impractical for the simulation of real structures. In this report, implementation focused on anisotropic thick shell elements to accept the load-displacement relations computed by the composite mechanics module as anisotropic plate or shell elements represent through-the-thickness properties of the composite and are more efficient than three-dimensional elements. After accepting the composite properties, the structural analysis module computes the strain and stress at each node in each ply. After each finite element stress analysis, the possible failure modes within each subvolume of each ply at each node of the composite structure are assessed by the following failure criteria:

$$\begin{aligned}
S_{f11C} &< \sigma_{f11} < S_{f11T} \\
S_{f22C} &< \sigma_{f22} < S_{f22T} \\
S_{f33C} &< \sigma_{f33} < S_{f33T} \\
S_{f12(-)} &< \sigma_{f12} < S_{f12(+)} \\
S_{f23(-)} &< \sigma_{f23} < S_{f23(+)} \\
S_{f13(-)} &< \sigma_{f13} < S_{f13(+)}
\end{aligned} \tag{1}$$

The stress limits in the above equations are computed by the composite mechanics module, based on constituent stiffness, strength, and fabrication process parameters. In addition to the first twelve failure modes, the thirteenth failure mode is a combined stress

or modified distortion energy (MDE) failure criterion (Chamis 1969) [14] that is obtained by modifying the usual distortion energy failure criterion expressed as

$$\left(\frac{\sigma_{\ell 11\alpha}}{S_{\ell 11\alpha}}\right)^2 + \left(\frac{\sigma_{\ell 22\beta}}{S_{\ell 22\beta}}\right)^2 - K_{\ell 12\alpha\beta} \frac{\alpha_{\ell 11\alpha}}{S_{\ell 11\alpha}} \frac{\sigma_{\ell 22\beta}}{S_{\ell 22\beta}} + \left(\frac{\sigma_{\ell 12S}}{S_{\ell 12S}}\right)^2 < 1 \quad (2)$$

Where  $\alpha$  and  $\beta$  indicate tensile or compressive stresses,  $S_{\ell 11\alpha}$  is the local longitudinal strength in tension or compression,  $S_{\ell 22\alpha}$  is the transverse strength in tension or compression, and the directional interaction factor  $K_{\ell 12\alpha\beta}$  is defined as:

$$K_{\ell 12\alpha\beta} = \frac{(1 + 4\nu_{12} - \nu_{13})E_{22} + (1 - \nu_{23})E_{11}}{[E_{11}E_{22}(2 + \nu_{12} + \nu_{13})(2 + \nu_{21} + \nu_{23})]^{1/2}} \quad (3)$$

For homogeneous isotropic materials, the directional interaction factor reduces to unity.

Once the damage modes at each node are assessed by the above failure criteria, a damage index is created to record the damage information for each damaged node. The damage index contains the node number, the ply number, and the list of damage criteria that have become activated. When a new failure occurs within a subvolume after a load increment, the damage index is updated correspondingly. The composite properties of each domain are degraded according to their damage index. If there is no damage after a load increment, the structure is considered to be in an equilibrium stage and an additional load increment is applied. If too many nodes are damaged and fractured during a load increment, incremental loads are reduced and the analysis is repeated from the previous equilibrium stage. Otherwise, if there is an acceptable amount of incremental damage, the constitutive properties and the structural geometry are updated to account for the damage and deformations in the previous increment. When damage is detected, the load increment is kept constant and applied on the updated finite element mesh leading to possible damage and fracture. Analysis is stopped when global structural fracture is predicted or the specimen is broken into two pieces.

To simulate the microstress level damage propagation, the matrix in orthotropic composite plies is subdivided into two regions, namely A and B [15]. Region A represents only the matrix that is not influenced by stress concentrations due to fiber interaction. Region B represents the fiber/matrix interaction zones. The ICAN module computes the microstresses in region A and B due to ply longitudinal, transverse, normal,



in-plane shear, out-of-plane shear stresses, temperature, and moisture. Damage progression module creates microstresses damage index as a binary number by comparison of microstresses with the tensile, compressive, and shear strength of the matrix. Fourteen regular failure modes of microstresses damage are included in both region A and B. The constituent level regional damage progression in specimens can be clearly described by the microstress damage index.

### **3.3 Simulation of coupons**

Unidirectional longitudinal tension specimens with embedded optical fibers were simulated using the CODSTRAN computer code. Composite laminates were made of Kevlar 49®/Epoxy with unidirectional and multidirectional configurations [16]. Optical fiber with core diameter of 100 $\mu$ m was embedded (1) parallel and (2) perpendicular to the unidirectional reinforcing fibers in the specimens and compared with reference coupon without embedment of optical fiber. In all cases, the pre-impregnated tapes were cured in an autoclave at 175°C under a pressure of 420 kN/m<sup>2</sup>. Fiber volume ratio was 0.61 and vacant volume ratio was less than 0.01.

To simulate different specimens using the CODSTRAN computer code, the resident databank with fiber/matrix properties were calibrated to match the experimental constituent properties. As discussed in the methodology, computer code ICAN has the ability of calculating the structure properties from separate fiber and matrix properties. One of the most important advantages using ICAN in this simulation is its ability of including the hygrothermal effects analysis on mechanical properties of composite structures.

#### **3.3.1. Reference tensile specimen without embedded optical fiber**

The reference specimen is simulated to calibrate the fiber/matrix properties under uniaxial tension test and provides fundamental laminate mechanical behavior to compare with other coupons. To evaluate the effects by embedded optical fiber on mechanical

properties in unidirectional tension tests and take into account the local effects of optical fiber, only central panel where there is embedded optical fiber is modeled in the simulation. The simulated part has the dimensions of 3.0mm×3.0mm×2.0mm. **Figure 3.1** shows the finite element model established to simulate the reference specimen with total 729 nodes and 676 Mindlin type rectangular elements. Boundary conditions of this finite element analysis are defined as in **Figure 3.2**. Along one of the edges all the nodes are constrained in Dx and Dz directions, and the middle node is also constrained in the Dy direction. All other nodes allow Dy-direction displacements. Along the other edge, all nodes can move in Dx, Dy,  $\theta_x$ , and  $\theta_y$  directions except the middle node constrained in Y direction. Unit loads are also applied at each node on this side to model the uniform tension stresses. To match the effectiveness of tab on the loading edge in mechanical tension test, all the nodes on the loading side are applied the same displacements along Dx direction as the middle node during each loading increment.

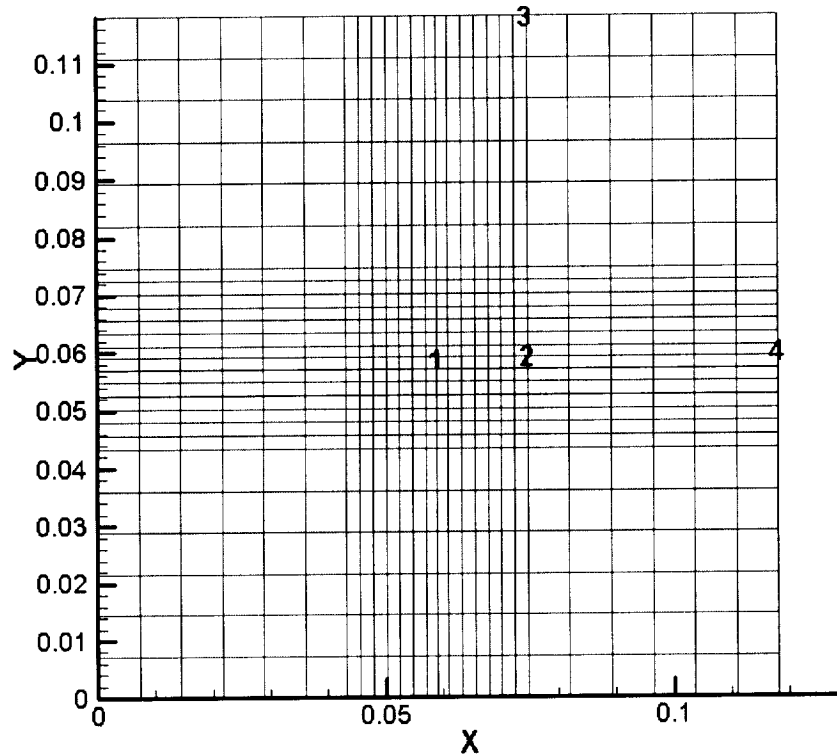


**Figure 3.1. Finite element mesh for the tension specimen**

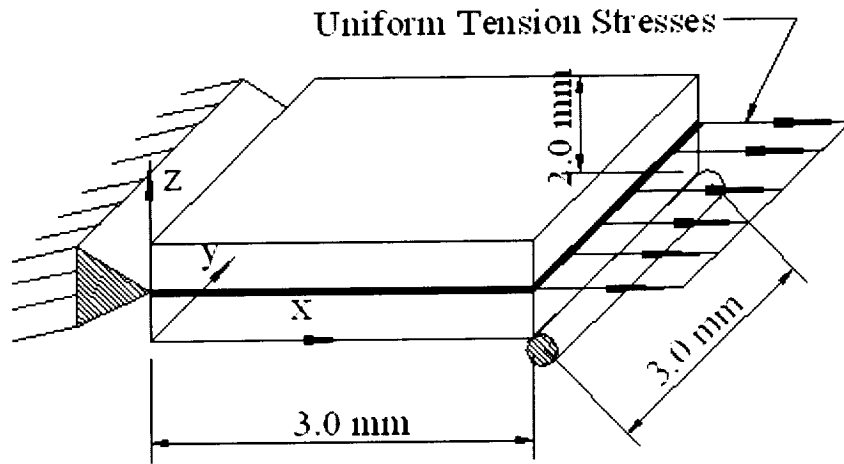


**Figure 3.2. Boundary conditions and specimen dimensions**

Elastic properties and hygrothermal properties of fiber/matrix and unidirectional laminates are obtained from the literature [16]. The strength properties are obtained by calibrating the specific finite element model of this reference coupon. **Table 3.1** and **Table 3.2** list the Kevlar fiber and epoxy matrix properties used in the simulation. The laminate properties computed by ICAN in **Table 3.3** are compared with the reference [16] provided results. Conclusions can be obtained from these three tables that are based on the simulation results of referenced unidirectional laminates, the elastic properties of laminates agree with the experimental data. Calibrated constituent strengths are different from the general literature provided value, which can be explained since constituent in-situ properties generally differ from their pristine state based on laminate data.

**Table 3.1. Kevlar 49® Fiber Properties**

	<b>Units</b>	<b>Simulation</b>	<b>General</b>
<b>Number of fibers per end</b>	—	768	768
<b>Fiber diameter</b>	$10^{-3}$ mm ( $10^{-3}$ in)	11.99(0.472)	—
<b>Fiber Density</b>	Kg/m <sup>3</sup> (lb/in <sup>3</sup> )	1451(0.0524)	1451(0.0524)
<b>Longitudinal normal modulus</b>	GPa ( $10^6$ psi)	124.79(18.1)	110~125*
<b>Transverse normal modulus</b>	GPa ( $10^5$ psi)	11.65(1.69)	—
<b>Poisson's ratio (<math>\mu_{12}</math>)</b>	—	0.345	0.36
<b>Poisson's ratio (<math>\mu_{23}</math>)</b>	—	0.150	—
<b>Shear modulus (<math>G_{12}</math>)</b>	GPa ( $10^6$ psi)	2.62(0.38)	—
<b>Shear modulus (<math>G_{23}</math>)</b>	GPa ( $10^6$ psi)	1.758(0.255)	—
<b>Longitudinal thermal expansion coefficient</b>	$10^{-6}/^{\circ}\text{F}$	3.6	—
<b>Transverse thermal expansion coefficient</b>	$10^{-6}/^{\circ}\text{F}$ ( $10^{-6}/^{\circ}\text{K}$ )	3.6(6.5)	3.6(6.5)*
<b>Longitudinal heat conductivity</b>	BTU-in/hr/in <sup>2</sup> / $^{\circ}\text{F}$	0.0193	—
<b>Transverse heat conductivity</b>	BTU-in/hr/in <sup>2</sup> / $^{\circ}\text{F}$	0.00193	0.00193
<b>Heat capacity</b>	BTU/lb/ $^{\circ}\text{F}$	0.0813	0.0813
<b>Tensile strength</b>	MPa (ksi)	2469(358)	3000(435)
<b>Compressive strength</b>	MPa (ksi)	517(75)	—

Note: \* from reference [16]; others from internet search

**Table 3.2. Epoxy Matrix Properties**

	<b>Units</b>	<b>Simulation</b>	<b>General</b>
<b>Matrix density</b>	Kg/m <sup>3</sup> (lb/in <sup>3</sup> )	1201(0.0434)	(0.0434)
<b>Normal modulus</b>	GPa (ksi)	3.57(517.5)	3.5 *
<b>Poisson's ratio</b>	—	0.36	0.36
<b>Coefficient of thermal expansion</b>	10 <sup>-6</sup> /°F(10 <sup>-6</sup> /°K)	33.3(60)	33.3(60)*
<b>Heat conductivity</b>	10 <sup>-3</sup> BTU-in/hr/in <sup>2</sup> /°F	8.681	8.681
<b>Heat capacity</b>	BTU/lb/°F	0.25	0.25
<b>Tensile strength</b>	MPa (ksi)	76.86(11.2)	70(10.2)
<b>Compressive strength</b>	MPa (ksi)	139.97(20.3)	140(20.3)
<b>Shear strength</b>	MPa (ksi)	119.97(17.4)	120(17.4)
<b>Allowable tensile strain</b>	—	0.05	0.05
<b>Allowable compressive strain</b>	—	0.052	—
<b>Allowable shear strain</b>	—	0.042	—
<b>Allowable torsional strain</b>	—	0.045	—
<b>Void heat conductivity</b>	BTU-in/hr/in <sup>2</sup> /°F	0.225	—
<b>Glass transition temperature</b>	°C (°F)	215.6(420)	215.6(420)

Note: \* from reference [16]; others from internet search

**Table 3.3. Mechanical Properties of Unidirectional Kevlar 49®/Epoxy Laminate**

	Units	Simulation	General
<b>Fiber volume fraction</b>	%	62	60±2*
<b>Longitudinal modulus</b>	GPa (10 <sup>6</sup> psi)	76.74(11.13)	80.3*
<b>Transverse modulus</b>	GPa (10 <sup>6</sup> psi)	7.74(1.123)	8.0*
<b>In-plane shear modulus</b>	GPa (10 <sup>6</sup> psi)	2.14(0.311)	2.1*
<b>Major Poisson's ratio</b>	—	0.3509	0.35*
<b>Longitudinal tensile strength</b>	MPa (ksi)	1491(216.2)	1280(185)
<b>Longitudinal compressive strength</b>	MPa (ksi)	312.3(45.3)	335(49)
<b>In-plane shear strength</b>	MPa (ksi)	89.9(13.04)	49(7.1)
<b>Transverse tensile strength</b>	MPa (ksi)	75.7(8.088)	30(4.2)
<b>Transverse compressive strength</b>	MPa (ksi)	101.1(14.66)	158(22.9)

Note: \* from reference [16]; others from internet search

For this reference specimen, when the total load was increased to the maximum equilibrium load of 1.85kip (8.229kN), the specimen could not endure loading increment anymore and node fractures occurred adjacent to the loading edge. After this loading stage, a little increment of loading broke the specimen into two parts suddenly due to the fiber tension failure mode. Ultimate strength computed from the ultimate loads was 1.379GPa. The specimen appeared to fail in a brittle fracture mode since no internal/surface damage was observed during each loading stage before the specimen's catastrophic fracture failure occurred. Final finite element mesh is shown in **Figure 3.3** after the specimen was broken into two parts.

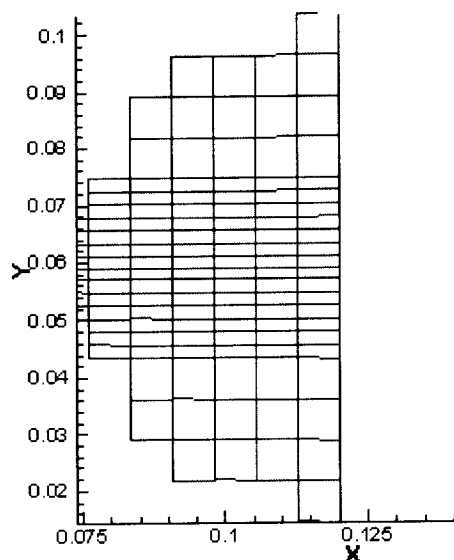


**Figure 3.3. Final finite element mesh for the reference coupon**

**Table 3.4. Glass Fiber Properties for Simulated Optical Fiber**

<b>Number of fibers per end</b>	—	204
<b>Fiber diameter</b>	$10^{-3}$ mm ( $10^{-3}$ in)	9.144(0.36)
<b>Fiber Density</b>	Kg/m <sup>3</sup> (lb/in <sup>3</sup> )	2491(0.09)
<b>Longitudinal normal modulus</b>	GPa ( $10^6$ psi)	85.5(12.4)
<b>Transverse normal modulus</b>	GPa ( $10^5$ psi)	85.5(12.4)
<b>Poisson's ratio (<math>\mu_{12}</math>)</b>	—	0.200
<b>Poisson's ratio (<math>\mu_{23}</math>)</b>	—	0.200
<b>Shear modulus (<math>G_{12}</math>)</b>	GPa ( $10^6$ psi)	35.6(5.17)
<b>Shear modulus (<math>G_{23}</math>)</b>	GPa ( $10^6$ psi)	35.6(5.17)
<b>Longitudinal thermal expansion coefficient</b>	$10^{-6}/^{\circ}\text{F}$	2.8
<b>Transverse thermal expansion coefficient</b>	$10^{-6}/^{\circ}\text{F}$	2.8
<b>Longitudinal heat conductivity</b>	BTU-in/hr/in <sup>2</sup> / $^{\circ}\text{F}$	0.052
<b>Transverse heat conductivity</b>	BTU-in/hr/in <sup>2</sup> / $^{\circ}\text{F}$	0.052
<b>Heat capacity</b>	BTU/lb/ $^{\circ}\text{F}$	0.17
<b>Tensile strength</b>	MPa (ksi)	2482(360)
<b>Compressive strength</b>	MPa (ksi)	2068(300)

### 3.3.2. Specimen with parallel embedment of optical fiber

To simulate the specimen with optical fiber parallel to reinforced Kevlar fibers, the same finite element mesh as in **Figure 3.1** was used. As a foreign object that is contained within the intraply region, the optical fiber is modeled using different lay-ups at different node locations. The general nodes of the finite element model have similar material lay-up as the reference specimen. However, the nodes containing optical fiber had specified slices to model the glass optical fiber. Hybrid material cards were computed by ICAN for the special elements. Although the optical fiber has larger diameter than the reinforcing Kevlar fibers, the parallel longitudinal configuration makes them associate well as reported in reference [16]. The laminate has consistent materials lay-up without installation speckles, and these two types of fibers are able to work well together in unidirectional laminates under longitudinal tension tests. General glass fiber properties in **Table 3.4** are used to simulate the optical fiber.

Computational simulation using the constituent material properties gave failure process details for the specimen with an optical fiber embedded parallel to the reinforcing fibers. When the loading increased to 1.73kip (7.70kN), damage initiation occurred along the nodes in the ply with embedded optical fiber due to the stresses that exceeded the longitudinal tension strength of these plies. Micro-mechanics level observation showed tension damage in the matrix region A, transverse tensile stress damage and shear stress damage in the fiber region B. Such failure types indicated matrix failure due to interaction caused damage between embedded optical fiber and composite laminate. Those nodes with damage are marked 'a' in **Figure 3.4**. With the incrementation of loading, failure extended along the optical fiber marked as 'b' to 'f'. When the load reached 1.87kip (8.318kN), the load could not be raised any more without fracturing the laminate structure. The nodes adjacent the loading edge fractured first, as in the reference coupon, and then, structural failure occurred due to fiber fractures when the total load reached 1.88kip (8.36kN). The final finite element mesh shown in **Figure 3.5** indicates that the optical fiber was also fractured. **Figure 3.6** shows the global damage percent during each loading stage. Although the scale of the plot in **Figure 3.6** shows a distinct increase in the damage growth, the absolute damage corresponding to global structure is relatively small ( $< 0.65\%$ ) and can be considered as the damage initiation stage. Also, the



damage only occurred and spread in several intraply layers and no obvious through-the-thickness fracture was observed before global failure. The structural failure is still a brittle fracture mode as it was for the reference specimen.

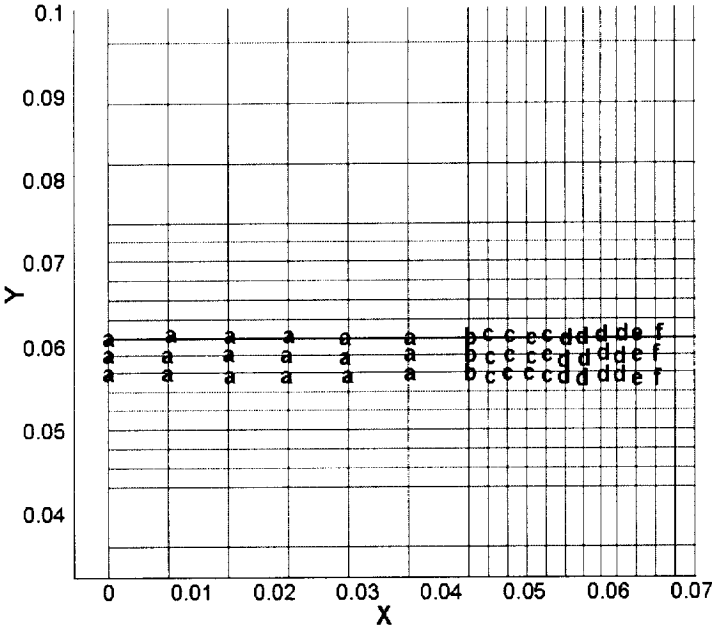


**Figure 3.4. Damage progression for coupon with embedded optical fiber parallel to reinforcing fibers**

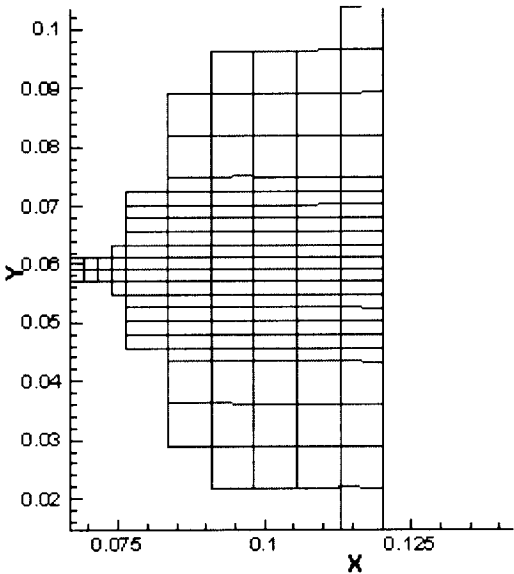


**Figure 3.5. Final finite element mesh for coupon with embedded optical fiber parallel to reinforcing fibers**

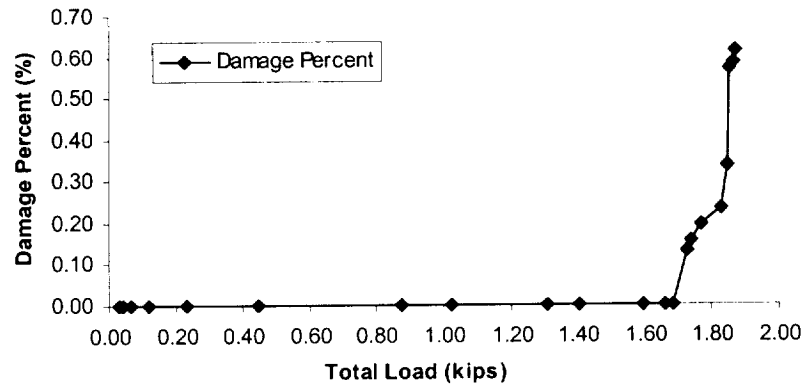


**Figure 3.6. Damage Percent vs. Load**

The Damage Energy Release Rate (DERR) is defined globally as the increment of work done by applied forces in each damage stage, per unit damage volume produced during structural degradation. The Total Damage Energy Release Rate (TDERR) is computed as the ratio of cumulative work done during the damage progression stages to the corresponding total damage volume. Both DERR and TDERR can be used to evaluate structural resistance against damage propagation at different loading stages. **Figure 3.7** shows the energy release rate as a function of tensile loading for the specimen with the embedded optical fiber parallel to reinforcing fibers. The two parameters have the same patterns in evaluating the structural fracture behavior. The higher values indicate the composite structure has more ability to prevent additional damage; on the other hand, the lower values of DERR and TDERR mean that the ability of the structure to resist damage is decreased. After the loading stage of 1.83kip corresponding to the peak value of the TDERR and DERR, the total number of damaged nodes decreased in each loading stage as the nodes marked ‘e’ and ‘f’ in **Figure 3.4**.

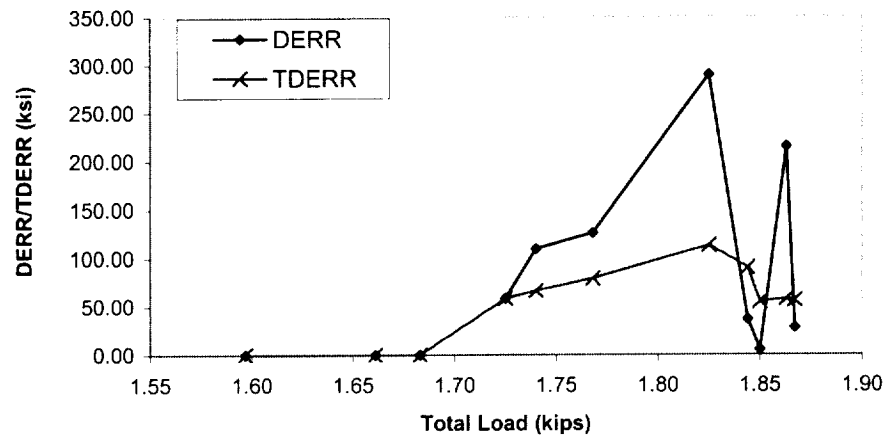


**Figure 3.7. Energy Release Rate vs. Load**

### 3.3.3. Specimen with perpendicular embedment of optical fiber

To compare the different specimens in this research, the same finite element mesh as in **Figure 3.1** was used to simulate the specimen with perpendicular embedment of optical fiber. As shown in reference [16], perpendicular embedment of optical fiber creates a resin wedge beside the optical fiber, the long axis of which is approximately six times the fiber-optic diameter. To simulate the perpendicular optical fiber installation caused resin area, the special material lay-ups around the optical fiber in **Figure 3.8** is used. Different constituent materials are considered. The material in the elements with notation 1 is the general reinforced Kevlar/Epoxy composite; the elements with notation 2 have hybrid composite materials: one is resin wedge having no reinforcing fibers considered; the other has a small fraction of 15% fibers and is the general Kevlar/Epoxy composite; the elements with notation 3 consist of only epoxy matrix. To model the part only containing epoxy matrix, an epoxy fiber with the  $0^\circ$  direction and the same properties as the epoxy matrix was hypothesized. The optical fiber is also modeled using hybrid materials as in the parallel embedment, but along  $90^\circ$  direction.

①	①	①	②	Optical Fiber	②	①	①	①
①	②	②	③		③	②	②	①
②	③	③	③		③	③	③	②
①	②	②	③		③	②	②	①
①	①	①	②		②	①	①	①

**Figure 3.8. Special elements for resin pocket in the specimen with embedded optical fiber perpendicular to the reinforcing fibers**

Damage progression for this specimen can also be described by computational simulation. Different from other two coupons, damage initiation occurred in the ply having perpendicular embedded optical fiber because of the transverse tension failure and longitudinal compression failure in the fibers when the load was very small at 39.4lb (175.3N). This failure was caused mainly by the micro-stress damage in region A of the matrix that also explained bond failure between optical fiber and resin matrix. Global damage over total structural volume is plotted as a function of applied total load at each loading stage in **Figure 3.9**. After the accumulation of damage around the optical fiber, the structure reached a new damage stability stage and experienced no additional damage under increased loading. When the load reached the value of 846lbs(3.763kN), damage occurred due to the failure of matrix in the resin pocket region 1 as shown in **Figure 3.8**. With the increased loading, damage spread from region 1 near the optical fiber to region 2 due to the matrix tension failure. When the load reached 878lb(3.906kN), the specimen achieved a second static damage stability stage. There was no additional damage except the damage in the resin pocket. When the total load reached 1.66kip(7.384kN), the structure was broken into two parts because of the tensile fracture of reinforcing fibers.

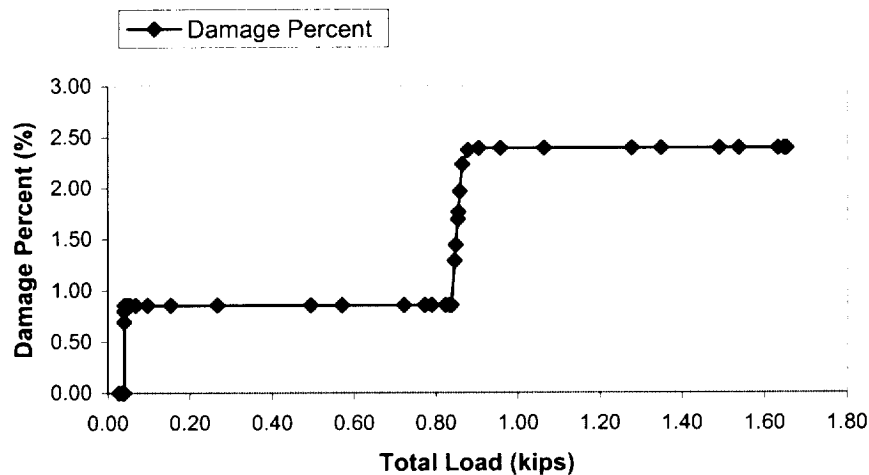


**Figure 3.9. Damage Percent vs. Total Load**

DERR and TDERR were also plotted as a function of total load as shown in **Figure 3.10**. After the matrix failure around the optical fiber and extension in the resin pocket, structural resistance to degradation reached its highest ability since the DERR and TDERR had the highest value. With the subsequent loading increments, the structure

maintained this characteristic and no additional damage was observed. After the load reached 1.63kip (7.25kN), the DERR and TDERR all suddenly decreased to a very low value and indicated the structural ability to resist damage propagation was reduced to the lowest level. After that stage, with a small increment of loading (133N), structural fracture occurred and the specimen was broken into two parts.

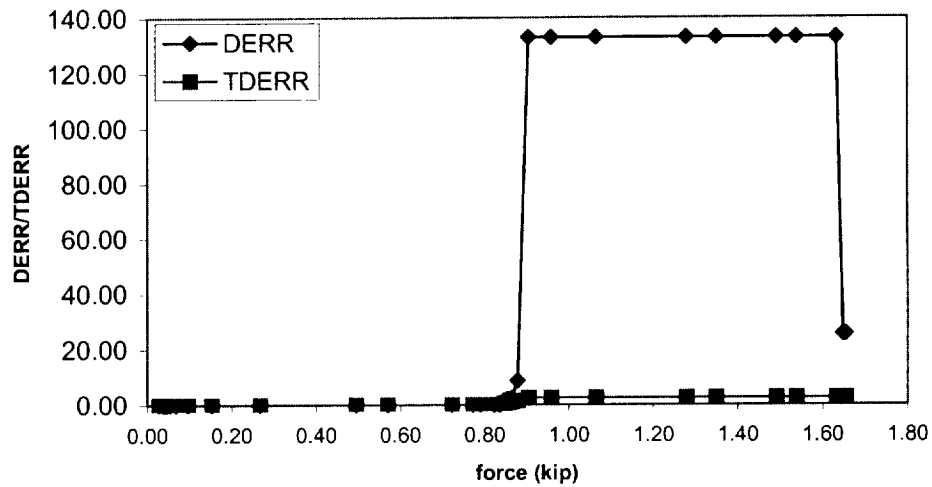


Figure 3.10. Energy Release Rate vs. force

### 3.4 Discussion

**Table 3.5** compares the ultimate strengths from simulation to those from experiments. The simulation achieves a good agreement of ultimate strength with experimental tests. As shown in **Table 3.5**, the embedment of optical fiber with a parallel configuration causes no influence on the ultimate strengths of unidirectional laminate in the uniaxial tension tests. On the contrary, due to the higher tensile strength of glass fiber, the ultimate strength of the laminate with parallel embedment of optical fiber increases about 1%. This supports the conclusion that embedment of optical fiber parallel to reinforcing fibers causes ignorable effects on the structural tensile strength in most of the experimental tests [1]. For the coupon with embedded optical fiber perpendicular to the reinforcing fibers, the ultimate tensile strength is reduced 10%. Detailed damage progression shows that the damage initiation occurred around the optical fiber and spread

quickly inside the resin pocket when the load was very small as only 2.37% of the ultimate loading. However, computational simulation indicates that the ultimate fracture load under monotonic loading is not significantly influenced by the appearance of matrix cracks [15]. **Table 3.6** compared the composite properties of three coupons. Composite elastic stiffness properties were displayed for different position and different specimens. The embedment of optical fiber causes little influence on the composite structural properties since the greatest reduction is about 4.5% for the longitudinal modulus and 2.3% for the transverse modulus. The major reason for the reduction of ultimate tensile strength can be explained in that the waviness of the reinforcing fibers around perpendicular embedded optical fiber causes reduction of tensile strengths of these fibers. Modification factors are used for different parts around the optical fiber in the simulation. Results show good agreement with the experimental tests taking account of these factors.

**Table 3.5. Comparison of Ultimate Strengths for Different Specimens between Simulations and Experiments (GPa)**

	Reference specimen	Parallel embedment of optical fiber	Perpendicular embedment of optical fiber
<b>Experiment (average)</b>	1.37	1.38	1.23
<b>Simulation</b>	1.379	1.393	1.231

**Table 3.6. Comparison of Composite Properties of Different Coupons**

	Reference specimen	Parallel coupon	Perpendicular coupon at optical fiber	Perpendicular coupon at resin pocket
<b>Longitudinal modulus (GPa)</b>	76.74	76.19	73.85	73.22
<b>Transverse modulus (GPa)</b>	7.743	8.122	10.673	7.557
<b>In-plane shear modulus (Msi)</b>	2.144	2.289	2.289	2.179
<b>Major Poisson's ratio</b>	0.351	0.342	0.2614	0.351

Although the three coupons had different damage progression characteristics, they all failed because of the fracture of the reinforcing fibers. Also, the specimens fractured suddenly without ductile deformation stages. They all displayed the characteristics of brittle materials. **Figures 3.11~3.14** depict the stress-strain relationships of four finite

element nodes as shown in **Figure 3.1** during the uniaxial tension tests. The linear relationship between stresses and strains at different locations in three diagrams show that the elastic behaviors of the tension specimens have little sensitivity to the embedded fiber-optic sensors with different configurations. The elastic moduli calculated from these four plots in **Table 3.7** have values that are close to the experimental tests and those computed directly by ICAN. An observation is also made that the perpendicular embedment of optical fiber induces a small reduction of the longitudinal elastic modulus.

**Table 3.7. Elastic Moduli Calculated from Structural Stress-Strain Relationship at different locations in Figure 3.11~3.14 (GPa)**

		Figure 3.11	Figure 3.12	Figure 3.13	Figure 3.14
<b>Elasticity modulus</b>	Reference coupon	75.9	75.9	76.8	76.2
	Parallel coupon	75.8	75.8	76.5	76.0
	Perpendicular coupon	74.9	74.4	75.2	75.2

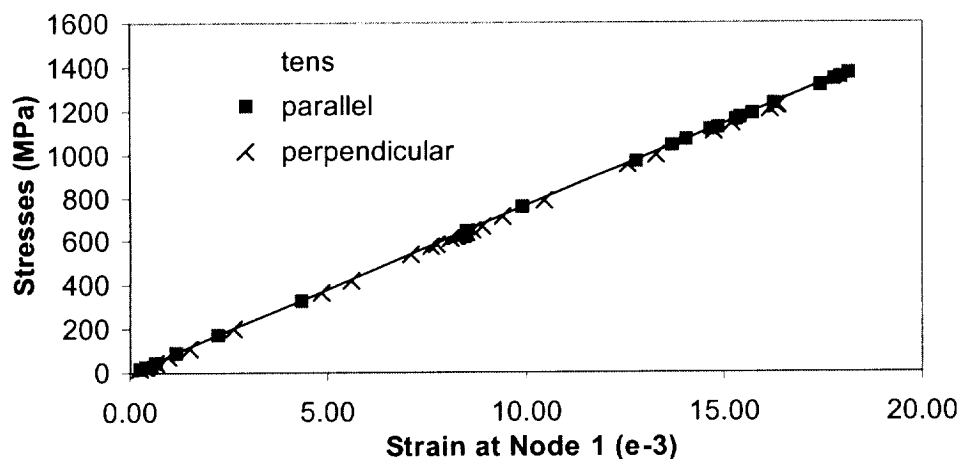


**Figure 3.11. Over Structural Stress-Strain Relationship at Node 1**

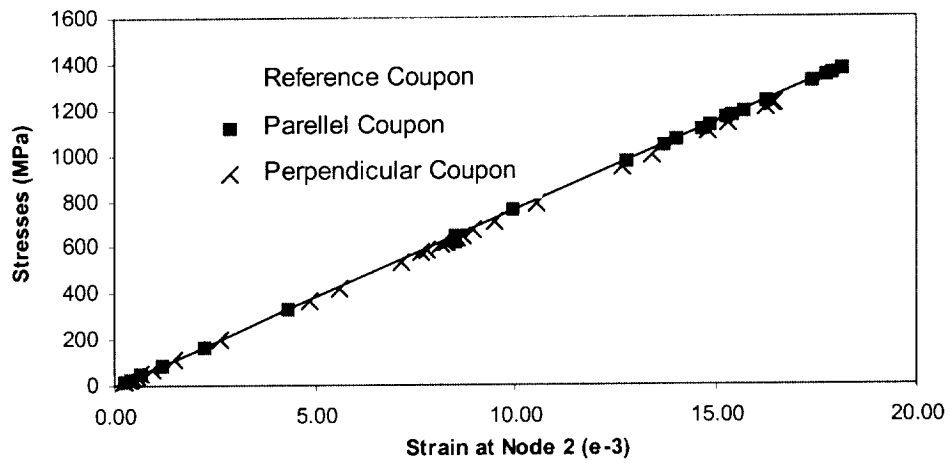


**Figure 3.12. Over structural Stress-Strain Relationship at Node 2**

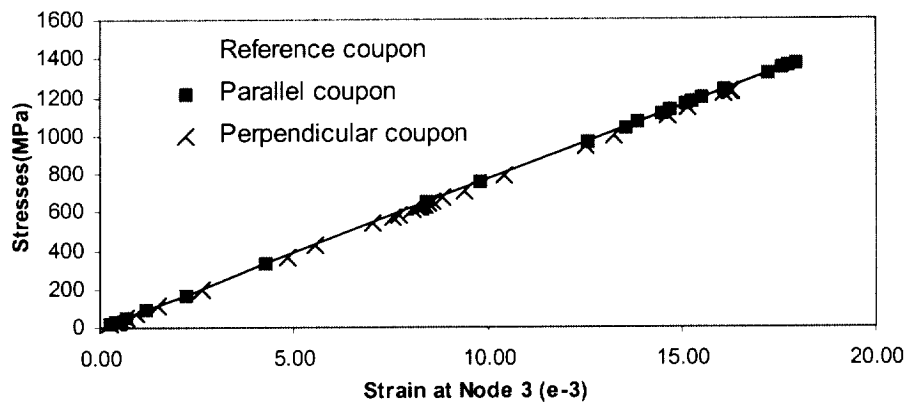


**Figure 3.13. Over Structural Stress-Strain Relationship at Node 3**



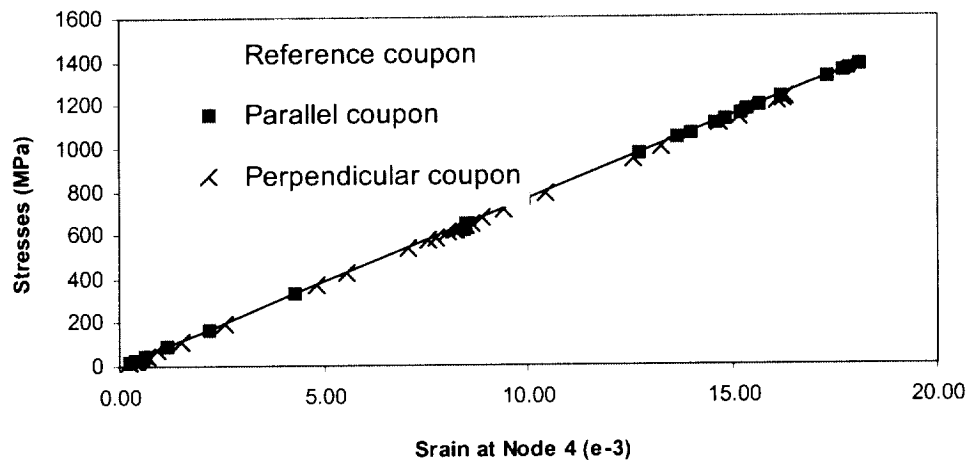


**Figure 3.14. Over Structural Stress-Strain Relationship at Node4**

### 3.5 Conclusions

Computational simulation method using CODSTRAN computer code was used to analyze the effects of embedded optical fiber with different configurations on the composite structural properties and damage progression for unidirectional laminates under uniaxial tension test. Optical fiber had configurations as parallel and perpendicular to the reinforcing fibers. The simulation results for ultimate strengths of different coupons match the experimental tests. The ultimate strength reduction for the specimen with perpendicular embedded optical fiber was also accurately predicted. Damage progression simulation at the micro-stress level quantified details of damage initiation, damage propagation and final structural fracture for different specimens. The specimen with perpendicular configuration of embedded optical fiber showed a much smaller damage initiation load compared to the others. A reduction of longitudinal elastic modulus was also simulated by both ICAN properties computation and final stress-strain relationships. Despite the differences of damage initiation among the three specimens, they all experienced brittle mode of failure because of similar sudden structural fracture and linear stress-strain relationships. Based on the present results, it has been

demonstrated that computational simulation helps to evaluate the embedded optical fiber effects on the mechanical behavior of composite structures, as well as provide a means to extend the CODSTRAN computer code to analyze progressive structural fracture behavior with residual defects caused by generally introduced containments that usually are unavoidable during *in situ* applications of manufactured composites.

### 3.6 References for Chapter III

1. Zhao, W. 2002 Test-Free Fracture Toughness, Final Report Chapter II.
2. Mauget, B.R., Minnetyan, L. and Chamis, C.C. 2001. "Computational Tracking of Composite Manufacturing with Fiber Preforms," *ASTM Journal of Composite Technology and Research*, Vol. 23, No. 4, pp. 254-258.
3. Minnetyan, L., Chamis, C.C. and Murthy, P.L.N. (1992). "Structural Behavior of Composites with Progressive Fracture," *Journal of Reinforced Plastics and Composites*, Vol.11, No. 4, pp.413-442.
4. Minnetyan, L. and Chamis, C.C. (1997). "Progressive Fracture of Composite Cylindrical Shells Subjected to External Pressure," *ASTM Journal of Composite Technology and Research*, Vol. 19, No. 2, pp. 65-71.
5. Minnetyan, L., Murthy, P.L.N. and Chamis, C.C. (1990a). "Composite Structure Global Fracture Toughness via Computational Simulation," *Computers & Structures*, Vol. 37, No. 2, pp.175-180.
6. Minnetyan, L., Murthy, P.L.N. and Chamis, C.C. (1990b). "Progressive Fracture in Composites Subjected to Hygrothermal Environment," *International Journal of Damage Mechanics*, Vol.1, No.1, pp 60-79.
7. Huang, D., Minnetyan, L. and P.E. Member, ASCE (1998). "Damage Progression in Carbon-Fiber Reinforced Plastic I-Beams", *Journal of Composites for Construction*, Vol. 2, No. 1, February, 1998, pp.38-45.
8. Huang, D., and Minnetyan, L. (2001). "Progressive Fracture of Stitched Stiffened Composite Shear Panels in the Postbuckling Range," *Journal of Reinforced Plastics and Composites*, Vol. 20, No.18, pp.1617-1632.
9. Minnetyan, L., and Chamis, C.C. (1997). "The Compact Tension, C(T), Specimen in Laminated Composite Testing," *Composite Materials: Fatigue and Fracture: ASTM STP*

- 1285, E.A. Armanios, Ed., American Society for Testing and Materials, 1997, pp. 531-550.
10. Chamis, C.C. and Smith, G.T. (1978). "Composite Durability Structural Analysis," NASA TM-79070, NASA-Lewis Research Center, Cleveland, OH.
  11. Murthy, P.L.N. and Chamis, C.C. (1986). "Integrated Composite Analyzer (ICAN): Users and Programmers Manual," NASA Technical paper 2515.
  12. Nakazawa, S., Dias, J.B. and Spiegel, M.S.(1987). "MHOST Users' Manual," NASA-Lewis Research Center, MARC Analysis Research Corp.
  13. Chamis, C.C. and Sinclair, J.H. (1979). "Micromechanics of Intraply Hybrid Composites: Elastic and Thermal Properties," NASA-TM-79253.
  14. Chamis, C.C. (1969). "Failure Criteria for Filamentary Composites," Composite Materials Testing and Design: *ASTM STP 460*, American Society for Testing and Materials, Philadelphia, pp.336-351.
  15. Zhang, H. and Minnetyan, L. and Chamis, C.C. and Abdi, F. 2001, "Microstress Level Damage Evaluation in Composite Structures", Published by Society for the Advanced of Material and Process Engineering with Permission.
  16. B. P. Arjyal, P. A. Tarantili, A. G. Andreopoulos and C. Galiotis, "Surface and bulk stress/strain measurements in composite laminates with a fibre-optic Raman probe," *Composites Part A: Applied Science and Manufacturing*, Volume 30, Issue 10, October 1999, Pages 1187-1195.